Regular Article – Experimental Physics

Photoproduction of $\pi^0\pi^0$- and $\pi^0\pi^+$-pairs off the proton from threshold to the second resonance region

F. Zehr[1], B. Krusche[1,a], P. Aguar[2], J. Ahrens[2], J.R.M. Annand[3], H.J. Arends[2], R. Beck[2,4], V. Bekrenev[5], B. Boillat[1], A. Braghieri[6], D. Branford[7], W.J. Briscoe[8], J. Brudvik[9], S. Cherepnya[10], R.F.B. Codling[3], E.J. Downie[3], P. Drexler[12], D.I. Glazier[7], L.V. Fil'kov[10], A. Fix[11], R. Gregor[12], E. Heid[2], D. Hornidge[13], I. Jaegle[1], O. Jahn[2], V.L. Kashevarov[10,2], A. Knezevic[14], R. Kondratiev[15], M. Korolija[14], M. Kotulla[1], D. Krambrich[2], A. Kulbardis[5], M. Lang[2,4], V. Lisin[15], K. Livingston[3], S. Lugert[12], I.J.D. MacGregor[3], D.M. Manley[16], Y. Maghrbi[1], M. Martinez[2], J.C. McGeorge[3], D. Mekterovic[14], V. Metag[12], B.M.K. Nefkens[9], A. Nikolaev[2,4], M. Ostrick[2], P. Pedroni[6], F. Pheron[1], A. Polonski[15], S. Prakhov[9], J.W. Price[9], G. Rosner[3], M. Rost[2], T. Rostomyan[6], S. Schumann[2,4], D. Sober[17], A. Starostin[9], I. Supek[14], C.M. Tarbert[7], A. Thomas[2], M. Unverzagt[2,4], Th. Walcher[2], D.P. Watts[7], and (The Crystal Ball at MAMI, TAPS, and A2 Collaborations)

[1] Department of Physics, University of Basel, Ch-4056 Basel, Switzerland
[2] Institut für Kernphysik, University of Mainz, D-55099 Mainz, Germany
[3] SUPA, School of Physics and Astronomy, University of Glasgow, G12 8QQ, UK
[4] Helmholtz-Institut für Strahlen- und Kernphysik, University Bonn, D-53115 Bonn, Germany
[5] Petersburg Nuclear Physics Institute, RU-188300 Gatchina, Russia
[6] INFN, Sezione di Pavia, I-27100 Pavia, Pavia, Italy
[7] School of Physics, University of Edinburgh, Edinburgh EH9 3JZ, UK
[8] Center for Nuclear Studies, The George Washington University, Washington, DC 20052, USA
[9] University of California Los Angeles, Los Angeles, California 90095-1547, USA
[10] Lebedev Physical Institute, RU-119991 Moscow, Russia
[11] Laboratory of Mathematical Physics, Tomsk Polytechnic University, Tomsk, Russia
[12] II. Physikalisches Institut, University of Giessen, D-35392 Giessen, Germany
[13] Mount Allison University, Sackville, New Brunswick E4L3B5, Canada
[14] Rudjer Boskovic Institute, HR-10000 Zagreb, Croatia
[15] Institute for Nuclear Research, RU-125047 Moscow, Russia
[16] Kent State University, Kent, Ohio 44242, USA
[17] The Catholic University of America, Washington, DC 20064, USA

Abstract. Precise total cross-sections and invariant-mass distributions have been measured for photoproduction of pion pairs off the proton producing $p\pi^0\pi^0$ and $n\pi^+\pi^0$ final states from the threshold region up to 800 MeV incident photon energy. Additionally, beam helicity asymmetries have been measured in the second resonance region (550 MeV–820 MeV). The experiment was performed at the tagged photon beam of the Mainz MAMI accelerator with the Crystal Ball and TAPS detectors combined to give an almost 4π solid-angle electromagnetic calorimeter. The results are much more precise than any previous measurements and confirm the chiral perturbation theory predictions for the threshold behavior of these reactions. In the second resonance region, the invariant-mass distributions of meson-meson and meson-nucleon pairs are in reasonable agreement with model predictions, but none of the models reproduce the asymmetries for the mixed-charge channel.

1 Introduction

The photoproduction of pion pairs has attracted a lot of interest over recent years in view of different properties of

[a] *Present address*: Klingelbergstrasse 82, CH-4056 Basel, Switzerland; e-mail: Bernd.Krusche@unibas.ch

the strong interaction. In particular, it can contribute to sensitive tests of chiral perturbation theory, to the investigation of non-ground-state decays of nucleon resonances via reaction chains like $R \to R'\pi \to N\pi\pi$ (R, R' nucleon resonances, $N = n, p$), and to the analysis of in-medium properties of hadrons like the σ-meson. The first topic is

related to the threshold behavior of double pion production off the nucleon, which has been predicted by chiral perturbation theory [1, 2]. The second is important for the extraction of nucleon resonance properties from the electromagnetic excitations of the proton and the neutron. Finally, the interpretation of modifications of the pion-pion invariant-mass distributions in nuclear matter requires input from the elementary reactions off the free nucleon.

Most of the recent progress in the theoretical treatment of the strong interaction comes from two different lines of research: 1) the development of the numerical methods of lattice gauge theory, approaching the nonperturbative regime downwards from large quark masses (see *e.g.* [3–5]) and 2) the methods of chiral perturbation theory (ChPT) [6, 7], extrapolating upwards from small momenta and vanishing quark masses. The latter, originally based on the approximate Goldstone boson nature of the pion and later extended to the nucleon sector [8,9], had a large success in correctly describing the threshold behavior of photon-induced π^0 production off the proton. Agreement with experiment [10–12] was achieved due to the contribution of pion loop diagrams, which were not considered in the derivation of the older low-energy theorems (LET). Subsequently, different observables in single pion photoproduction have been measured and interpreted in the framework of chiral perturbation theory. Examples are the unitary cusp in the s-wave E_{0+} multipole of π^0-photoproduction at the π^+ production threshold [13] and the polarizability of the charged pion [14] studied via the $\gamma p \to \gamma \pi^+ n$ reaction. In the meantime, it was discovered [1, 2] that the chiral loop diagrams play an even more important role for double pion production, opening a new door for ChPT tests. An unexpected prediction was that, very close to threshold, the double π^0 channel is so much enhanced by loop corrections that its cross-section rises above the charged and mixed-charged channels. This is completely counterintuitive. At higher incident photon energies the reactions involving pairs with charged pions ($\pi^0\pi^+$, $\pi^-\pi^+$) have much larger cross-sections, and in single pion production in the threshold region, the $p\pi^0$ final state is strongly suppressed with respect to $n\pi^+$. However, in double pion production, although contributions of order one vanish for neutral pion pairs, the corrections of order M_π are predicted to be much larger than for the pairs with charged pions [2]. This result is stable when all next-to-leading-order terms of order M_π^2 are considered. At this order also resonance contributions come into play via the $N^\star N\pi\pi$ s-wave vertex. The largest contribution by far involves the $P_{11}(1440)$ resonance. Taking all contributions together, the leading-order chiral loop diagrams contribute roughly 2/3 of the total $2\pi^0$ yield, making this channel the ideal testing ground for these contributions, which in most other reactions account only for small corrections. The calculations [2] predict the following threshold behavior for $\gamma p \to p\pi^0\pi^0$:

$$\sigma_{\text{tot}}(E_\gamma) = 0.6\,\text{nb} \cdot \left(\frac{E_\gamma - E_\gamma^{\text{thr}}}{10\,\text{MeV}} \right)^2, \qquad (1)$$

where E_γ is the incident photon energy in MeV and $E_\gamma^{\text{thr}} = 308.8\,\text{MeV}$ is the production threshold. The largest uncertainty in this prediction comes from the s-wave coupling of the $P_{11}(1440)$ resonance, which was taken from an analysis of the $\pi N \to \pi\pi N$ reaction [15]. Equation (1) uses the central value of this coupling. If instead the upper limit is used, the coefficient in the equation rises from $0.6\,\text{nb}$ to $0.9\,\text{nb}$.

The threshold behavior of double π^0 production was also investigated in the framework of the Gomez Tejedor-Oset (Valencia) model [16]. Here, it was found [17] that the low-energy cross-section is considerably enhanced when final-state interaction (FSI) contributions are taken into account in addition to the pure tree level treatment in [16]. In particular the re-scattering of $\pi^+\pi^-$-pairs produced via the Δ-Kroll-Ruderman diagram into $\pi^0\pi^0$ gives a considerable contribution. Altogether, the FSI effects almost double the threshold cross-section for the $2\pi^0$ channel, which can be regarded as a kind of remnant of the chiral loop effects discussed above. However, very close to threshold, their final result is still smaller than the values predicted by the chiral theory.

At higher incident photon energies, double pion production is of interest in view of the decay of nucleon resonances. It is a well-known problem that far fewer nucleon resonances have been observed in experiments than are predicted by quark models. A possible explanation could be the experimental bias against states that couple only weakly to $N\pi$, introduced into the data base by the dominance of elastic pion scattering experiments. Photon-induced reactions can remove this bias for the initial state, but then final states other than $N\pi$ must be investigated. As discussed in detail in [18] three alternative decay modes of nucleon resonances can be studied via double pion production: the sequential decay via an intermediate excited nucleon state (for all types of pion pairs), the decay into the $N\rho$ channel (for $\pi^0\pi^+$ or $\pi^+\pi^-$) and the emission of the σ-meson (for $\pi^0\pi^0$ or $\pi^+\pi^-$). The reaction $\gamma p \to p\pi^0\pi^0$ has been recently investigated in detail in view of such resonance contributions with the Bonn-Gatchina (BoGa) coupled-channel model up to incident photon energies of $1.3\,\text{GeV}$ [19, 20].

Much more data are available at lower incident photon energies in the second resonance region comprised of the $P_{11}(1440)$, $S_{11}(1535)$, and $D_{13}(1520)$ states. Total cross-sections and invariant-mass distributions of the $\pi\pi$- and the πN-pairs have been measured with the DAPHNE and TAPS detectors at the MAMI accelerator in Mainz [21–28], at GRAAL in Grenoble (also linearly polarized beam asymmetry) [29, 30], and with the CLAS detector at JLab (electroproduction) [31]. Recently polarization observables were also measured at the MAMI accelerator [32–36] and at the CLAS facility [37]. However, it is somewhat surprising that, despite all these efforts, the interpretation of the data is still controversial even at low excitation energies, where only a few well-known resonances contribute. All models agree that the production of charged pions involves larger background contributions from non-resonant terms like pion-pole diagrams or terms of the Δ-Kroll Rudermann type. The extreme cases are

the $\pi^+\pi^-$ final state, which at moderate incident photon energies is dominated by such contributions, and the $\pi^0\pi^0$ final state with only small background contributions. The latter is thus better suited for the study of resonance contributions.

However, the reaction models do not even agree for the dominant contributions to double π^0 production. In the model of the Valencia group [16,38,39] the most important contribution comes from the $D_{13}(1520) \to \Delta\pi^0 \to p\pi^0\pi^0$ reaction chain. In the model of Laget and co-workers [29] a much more prominent role is played by the $P_{11}(1440) \to N\sigma$ decay. The recent Bonn-Gatchina analysis finds a large contribution from the $D_{33}(1700)$ state, which is almost negligible in the other models. The effective Lagrangian model from Fix and Arenhövel (Two-Pion-MAID [40]) is also dominated by the D_{13} resonance, but strongly underestimates the total cross-section at incident photon energies below $700\,\mathrm{MeV}$. The results for the helicity dependence of the cross-sections obtained from the experiments on the Gerasimov-Drell-Hearn sum rule [32–34] show a dominance of the $\sigma_{3/2}$ component. This is in line with the excitation of D_{13} or D_{33} resonances and limits possible P_{11} contributions.

The situation is even more complicated for the mix-charged $n\pi^0\pi^+$ and $p\pi^0\pi^-$ final states. Early model calculations in the framework of the Valencia or the Laget model (see, *e.g.*, [16]) could not even reproduce the total cross-section. First experimental data for the invariant-mass distributions of the pion pairs [24,27] indicated an enhancement at large invariant masses, which was interpreted as a possible contribution from ρ-mesons, *e.g.*, via the $D_{13}(1520) \to N\rho$ decay. Introduction of this process into the models improved substantially the agreement with experiment [38–40].

The behavior and interpretation of the low-energy double pion production reactions are also relevant for different aspects of the much discussed in-medium properties of hadrons. The above-mentioned coupling of the $D_{13}(1520)$ resonance to the $N\rho$ channel has been discussed in [27] as a possible explanation of the strong suppression of the second resonance bump in total photoabsorption by nuclei [41]. For the free nucleon this structure is dominated by this D_{13} resonance. If it couples strongly to $N\rho$ and the ρ is broadened or shifted to lower mass in nuclear matter, then also the nucleon resonance will be broadened and the bump structure will be suppressed for nuclei. The study of the line shape of this resonance via single π^0 photo-production off nuclei could not establish such a nuclear broadening [42]. However, the interpretation of the data is greatly complicated by final-state interaction effects.

The other important in-medium effect discussed in the context of low-energy double pion production is the behavior of the σ-meson in nuclear matter. The masses of the $J^\pi = 0^-$ pion and its chiral partner the $J^\pi = 0^+$ σ-meson are very different in vacuum, which is a well-known manifestation of chiral symmetry breaking. The masses should become degenerate in the chiral limit, so that one naively expects a density dependence of the mass due to partial chiral restoration effects. Results [43] obtained in the framework of the Nambu-Jona-Lasinio model indicated in-

deed a strong drop of the σ mass as a function of nuclear density which is already significant at normal nuclear density ρ_0 at which the pion mass remains stable. The predicted effect for the production of meson pairs off nuclei is a downward shift of the invariant-mass distributions of scalar isoscalar meson pairs. This prediction has been experimentally investigated with pion- and photon-induced double pion production reactions [44–51]. The CHAOS Collaboration [44–48] reported such a downward shift for $\pi^+\pi^-$-pairs with respect to $\pi^+\pi^+$-pairs from pion-induced reactions. The Crystal Ball Collaboration at BNL [49] observed a low-mass enhancement of strength for heavy nuclei in π^--induced $\pi^0\pi^0$ production. In photon-induced reactions, a downward shift of the invariant-mass distributions of $\pi^0\pi^0$-pairs with respect to $\pi^0\pi^\pm$-pairs has been measured by the TAPS Collaboration [50,51]. However, intricate final-state interaction effects [51] complicate the interpretation of the results. They require detailed studies in the framework of models, which have to rely on precise input for the elementary cross-sections off the free nucleon, in particular at low incident photon energies.

The present paper reports a simultaneous, precise measurement of the total cross-section and the invariant-mass distributions of the $\gamma p \to p\pi^0\pi^0$ and $\gamma p \to n\pi^0\pi^+$ reactions from as close as possible to threshold up to the second resonance region. In addition, the use of a circularly polarized photon beam allowed the measurement of the beam-helicity asymmetry as a function of the azimuthal angle between the reaction and production planes. The results for this asymmetry, which are very sensitive to details of the reaction models, have already been published in a preceding letter [36].

The paper is organized as follows. A brief description of the experimental setup is given in sect. 2. The data analysis, including calibration procedures, particle identification, Monte Carlo simulations of the detector response, and estimates of systematic uncertainties, is summarized in sect. 3. In sect. 4 (Results) first the threshold region is discussed, particularly in view of chiral perturbation theory predictions, followed by a comparison of the results from several reaction models to the observables at higher incident photon energies.

2 Experimental setup

The experiment was performed at the Mainzer Mikrotron (MAMI B) accelerator [52,53] using the Glasgow tagging spectrometer [54,55] and an almost 4π covering electromagnetic calorimeter combining the TAPS [56,57] and Crystal Ball (CB) [58] detectors. Here we give only a short summary of the main parameters of the setup. Details can be found in [59], which used the same data set for the investigation of the $\gamma p \to p\pi^0\gamma'$ reaction.

A schematic drawing of the main components of the detector system is shown in fig. 1. The data were taken with a $4.8\,\mathrm{cm}$ long liquid-hydrogen target, which was mounted from the upstream side in the center of the Crystal Ball. The Ball is composed of 672 NaI crystals covering the full azimuthal range for polar angles between $20°$
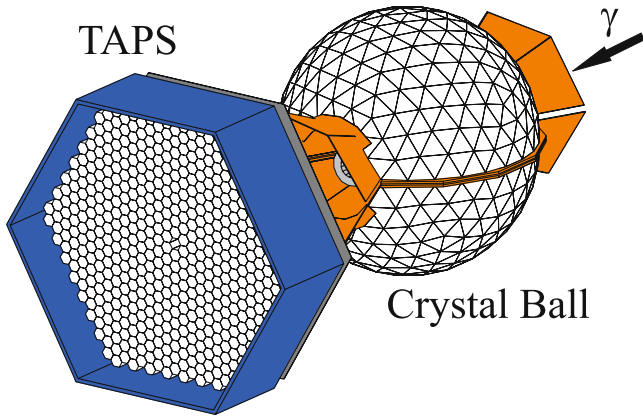
Fig. 1. Experimental setup of the electromagnetic calorimeter consisting of TAPS and Crystal Ball detector. Detectors for charged particle identification are mounted inside the Crystal Ball around the target (PID and MWPCs) and in front of the TAPS forward wall (TAPS veto-detector).

and 160°. A Particle Identification Detector (PID) [60] (24 plastic scintillator bars of 31 cm length, 13 mm width and 2 mm thickness) and two cylindrical multiple wire proportional chambers (MWPCs) [61] were mounted inside the Ball in cylindrical geometry around the target, covering the same polar angle range. The forward angular range from 20° down to 1° was covered by the TAPS detector [56,57] with 510 BaF$_2$ crystals arranged as a hexagonal wall and placed 1.75 m downstream from the target. Each module of this detector had an individual plastic scintillator (5 mm thickness) of the same hexagonal geometry in front for the identification of charged particles.

The energy resolution for electromagnetic showers of both CB and TAPS is approximately given by [57,58]

$$\frac{\sigma_E}{E} \approx \frac{2-3\%}{\sqrt[4]{E/\text{GeV}}}. \qquad (2)$$

A more precise parameterization for TAPS can be found in [57]. The angular resolution was better than 1° FWHM for TAPS and FWHM$_\Theta$ = 4.5°–7° for polar and FWHM$_\phi$ = FWHM$_\Theta$/ sin(Θ) for azimuthal angles in the CB.

The photon beam with energies up to 820 MeV was produced by bremsstrahlung from the 883 MeV electron beam of the MAMI accelerator. The energy of the incident photons was determined event by event by the Glasgow photon tagger [54,55] with an energy resolution of approximately 2 MeV full width. The electron beam was longitudinally polarized with a polarization degree of $(82 \pm 5)\%$ so that the photon beam carried a circular polarization determined by the photon-energy–dependent polarization transfer factor [62]. The incident photon flux was derived from the number of deflected electrons per tagger channel, which were counted with life-time gated scalers. The tagging efficiency, *i.e.* the fraction of correlated photons that pass through the collimator and impinge on the target, was periodically determined with special tagging ef-

ficiency runs. This was done by measuring directly the photon beam intensity with a total absorbing lead-glass counter, which was moved into the photon beam at reduced intensity. During the normal data-taking runs the photon beam intensity was monitored in arbitrary units with an ionization chamber at the end of the beam line. After normalization to the tagging efficiency runs these data were used to correct the time dependence of the tagging efficiency, which however was quite stable (varying between 30%–34%).

3 Data analysis

### 3.1 Particle identification and reconstruction

In general, electromagnetic showers produce signals in extended "clusters" of detector modules in the calorimeters. The first step of the analysis therefore combined all hits of adjacent crystals into "clusters" and determined their energy sums and their energy weighted geometrical centers of gravity. In the next step these "clusters" were assigned to different particle types with the methods discussed below.

3.1.1 TAPS forward wall with veto-detector

The response of the TAPS-detector to electromagnetic showers originating from photons is discussed in detail in [57]. The separation between photons, charged pions, and recoil nucleons in TAPS is based on three methods. The plastic scintillators from the veto-detector distinguish between charged and neutral hits. A hit was assigned as charged when the veto of any module in the cluster or the veto of any neighbor of the central module (module with highest energy deposit) had fired (even if the neighbor module itself had no signal above threshold). The latter condition applies to cases where a charged particle with large impact angle passed through the edge of a veto and then deposited its energy in a neighboring BaF$_2$ module.

Photons and recoil nucleons can be separated by a pulse-shape analysis (PSA) based on the scintillation properties of BaF$_2$. The crystals emit scintillation light at two different wavelengths with very different decay constants ($\tau_f = 0.76$ ns, $\tau_s = 620$ ns) and the intensity ratio of the two components depends on the nature of the incident radiation. This is routinely explored by integrating the output signals over a short (≈ 50 ns) and a long ($\approx 2\,\mu$s) gate period. The two energy signals were calibrated in a way that in a plot of long- *versus* short-gate signal photons appear along the 45° line. Since the fast component is suppressed for recoil nucleons, they appear at smaller angles (see insert in fig. 2). For practical purposes the signals were parameterized in polar coordinates R, ϕ via

$$R = \sqrt{(E_l^2 + E_s^2)}, \qquad \phi = \tan^{-1}\left(\frac{E_s}{E_l}\right), \qquad (3)$$
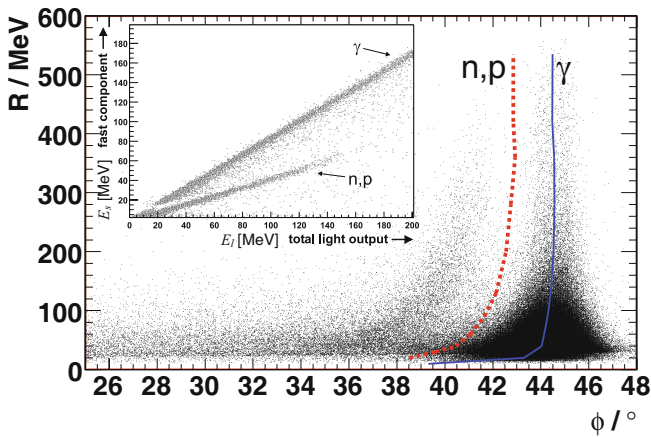
Fig. 2. (Color online) Pulse-shape analysis for the TAPS detector. The insert shows the signal integrated over a short-gate time *versus* the total signal. The main plot shows the pulse-shape signal in polar coordinates. Solid (blue) line: position of photon peak. Dashed (red) line: 3σ limit cut between photons and nucleons.
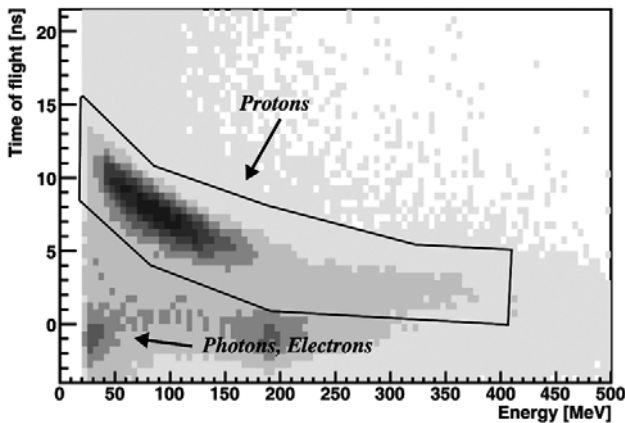
Fig. 3. Time of flight *versus* energy analysis for nucleons detected in TAPS. The offset of the time calibration is such that photons appear at zero time of flight.

where E_s, E_l are the short- and long-gate energy signals. The cut for the identification of photons was then defined in small slices of the spectra in the radius R projected onto the ϕ-axis. These spectra were fitted by Gaussian peaks plus a first-order background polynomial (see [63] for details). The solid (blue line) in fig. 2 indicates the position of the Gaussian peaks and the dashed (red) line the 3σ limit. Entries at the right-hand side of the dashed line were accepted as photons.

A further possibility to separate protons and photons in TAPS is a time of flight *versus* energy analysis. This is demonstrated in fig. 3. The selected events had exactly two photons in the Crystal Ball with an invariant mass close to the π^0 mass and one further hit in TAPS. This means that, apart from small background contributions, the reaction $\gamma p \to p\pi^0$ with the recoil proton in TAPS was
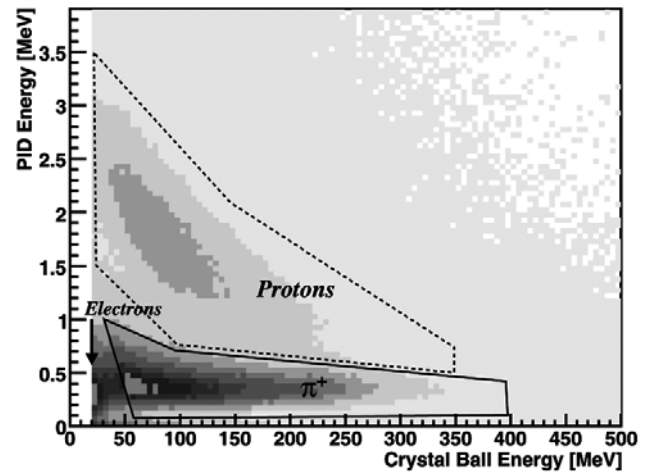
Fig. 4. $\Delta E - E$ analysis using CB and PID. The energy deposition in the PID is plotted *versus* that in the CB.

selected. In the figure the difference between the average time of the two photons and the time of flight for the hit in TAPS is plotted *versus* the energy deposited by the hit in TAPS. Proton hits are confined in a well-defined curved zone. The indicated limits define which hits are assigned as protons. The PSA and time of flight *versus* energy analysis are complementary since the first is most efficient for large proton energies, while the latter is optimal for the smallest energies. In principle, it is possible to identify with these tools photons, neutrons, protons, and charged pions (see [51] for details, the pions form a separate band in the time of flight *versus* energy spectra). However, as discussed in sect. 3.2, for the present analysis they were only used to identify a very clean sample of photons in TAPS.

3.1.2 Crystal Ball with PID and MWPCs

Charged particles hitting the CB must traverse the PID and the MWPCs. The PID was used to identify protons and charged pions. This was done by a $\Delta E - E$ analysis that compared the differential energy loss of the particles in the PID to the total deposited energy in the CB. A typical spectrum is shown in fig. 4. The bands for protons and charged pions are clearly separated.

The energy deposition of hadrons spreads over fewer detector modules than electromagnetic showers and in many cases the energy deposit is confined to a single crystal. This means that the angular resolution for hadrons ($\approx 10°$ for Θ) is worse than for photons for which the center of gravity of the extended cluster defines the impact point better than the detector granularity. Therefore, for charged particles the angular information from the CB was replaced by the tracking information delivered by the MWPCs whenever such information was available (if not the reconstruction from the CB clusters was used). Using the intersection points of the particle trajectory with the

two MWPCs an angular resolution of $\text{FWHM}_\Theta = 3°\text{--}5.5°$ and $\text{FWHM}_\phi = 3.3°$ was obtained. The angular resolution and the detection efficiency of the MWPCs was experimentally determined with penetrating cosmic muons and the reactions $\gamma p \to p\pi^0$ and $\gamma p \to n\pi^+$. For the latter two, events with protons, respectively, charged pions, identified by the $E - \Delta E$ analysis were selected and it was measured for which fraction of those events the MWPCs had responded. The total efficiency of the MWPCs determined this way was 90% for protons 79% for π^+-mesons. Note, however, that this efficiency does not directly enter into the total detection efficiency since π^+-mesons without MWPC information were not discarded but had only a moderately lower angular resolution form the CB cluster reconstruction (see sect. 3.3 for details of the efficiency simulations).

3.2 Reaction identification

3.2.1 The reaction $\gamma p \to p\pi^0\pi^0$

For this reaction events with exactly four neutral hits and one or no candidate for the recoil proton were accepted. Photons and proton (if detected) had to fulfill the above-discussed identification criteria. Detection of the recoil protons was not required for two reasons. Protons from reactions at low incident photon energies have low kinetic energies and were mostly stopped in the target or other material. Requiring proton hits would have drastically reduced the overall detection efficiency and would have not allowed a measurement of the reaction close to threshold. At higher incident photon energies, protons were detected with good detection efficiencies. However, when the detection of the proton is required, the simulation of the detection efficiency becomes more involved and more model dependent. This would have unnecessarily introduced an additional systematic uncertainty.

The accepted events were subjected to a combined invariant and missing-mass analysis. In the first step, the four photons were combined into the three possible disjunct pairs. For each of the combinations the invariant mass of the two pairs was calculated and the "best" combination was chosen with a χ^2 test minimizing

$$\chi^2 = \sum_{k=1}^{2} \frac{(m_{\gamma\gamma}(k) - m_{\pi^0})^2}{(\Delta m_{\gamma\gamma}(k))^2}, \qquad (4)$$

where m_{π^0} is the pion mass and the $m_{\gamma\gamma}$ are the invariant masses of the photon pairs with their uncertainties $\Delta m_{\gamma\gamma}$. The two-dimensional spectrum of the invariant masses of the best combinations in fig. 5 shows a clear peak at the position of the π^0 invariant mass. The small background under the peak was determined from a side-bin analysis and subtracted.

Subsequently, the nominal mass of the pion was used to improve the resolution. Since the angular resolution of the detector system is much better than the energy resolution
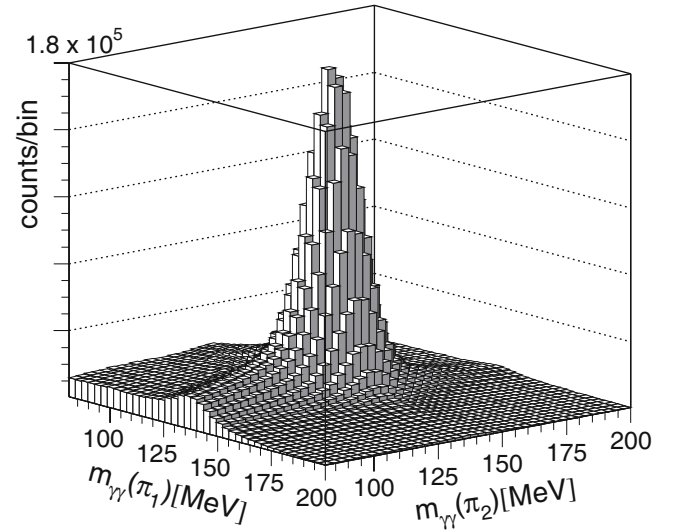
Fig. 5. Invariant masses of the "best" combination of four photons to two pairs for the $\gamma p \to p\pi^0\pi^0$ reaction.
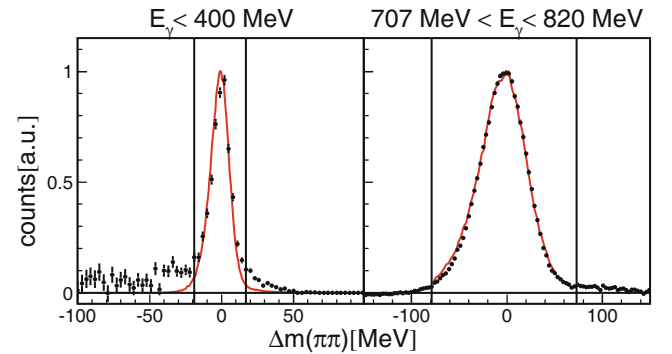
Fig. 6. (Color online) Missing-mass spectra for the $\gamma p \to p\pi^0\pi^0$ reaction in the threshold range and at high incident photon energies. The solid (red) histograms are GEANT simulations of the detector response. Vertical lines indicate the applied cuts.

this was simply done by replacing the measured photon energies by

$$E'_{1,2} = E_{1,2} \frac{m_{\pi^0}}{m_{\gamma\gamma}}, \qquad (5)$$

where $E_{1,2}$ are the measured photon energies, $E'_{1,2}$ the recalculated energies, m_{π^0} is the nominal π^0 mass, and $m_{\gamma\gamma}$ the measured invariant mass.

In the final step of the analysis the mass of the recoil proton, which was treated as missing particle regardless of whether it was detected or not, was compared to the missing mass of the reaction using

$$\Delta m(\pi\pi) = \left| P_\gamma + P_p - P_{\pi_1^0} - P_{\pi_2^0} \right| - m_p, \qquad (6)$$

where m_p is the nucleon mass, P_γ, P_p, $P_{\pi_{1,2}^0}$ are the four-momenta of the incident photon, the initial-state proton (which was at rest), and the produced π^0-mesons. The results for the two most critical energy regions —close to threshold and at highest incident photon energy— are shown in fig. 6. The critical point in the threshold region is

the very low cross-sections of double π^0 production. However, the spectrum shows a rather clean peak. At higher incident photon energies, earlier experiments [22,25] were plagued by background from the $\eta \to 3\pi^0$ decay. The large solid angle coverage of the present experiment results in a negligible probability to lose two out of six photons so that this background did not contribute significantly. Only a tiny remnant signal is visible around missing masses of +100 MeV.

In the final step, the kinetic energy and momentum of the recoil proton (no matter if detected or not) were reconstructed via the overdetermined reaction kinematics from the incident photon energy and the measured momenta of the two pions.

3.2.2 The reaction $\gamma p \to n\pi^0\pi^+$

For this reaction events with two or three neutral hits and a charged hit in the CB were selected. Detection of the recoil neutron was allowed but not required. The charged hit in the CB had to pass the $\Delta E - E$ analysis as a charged pion. Charged pions in TAPS were not considered. The reason is that the identification via the $\Delta E - E$ analysis using the PID was cleaner than the identification in TAPS where only time of flight *versus* energy could be used to distinguish charged pions from protons (charged pions would appear in fig. 3 between protons and photons; see [51] for details). Since protons misidentified as charged pions were the most important background source (see below), events with charged-pion candidates in TAPS were discarded. This introduced of course an additional systematic uncertainty into the simulation of the detection efficiency since a small part of the solid angle was not covered.

In the first step of the analysis the invariant mass of the photon pair was calculated. When three neutral hits had been detected in the CB, where neutrons and photons cannot be distinguished, again the best combination was chosen. The resulting invariant-mass spectrum was very clean and a cut was applied for invariant masses between 115 MeV and 160 MeV. As for the double π^0 channel the nominal mass of the π^0 was then used to recalculate the photon energies from eq. (5).

Treating again the recoil nucleon as a missing particle, the missing mass can be calculated from eq. (6), replacing one of the π^0-mesons by the π^+ and the final-state nucleon by the neutron. The result is shown in the center row of fig. 7. The peaks around zero correspond to the $\gamma p \to n\pi^0\pi^+$ reaction. The background level is quite high, especially in the threshold region. The problem arises from protons from the $\gamma p \to p\pi^0$ reaction that leak in the $\Delta E - E$ analysis (see fig. 4) into the π^+ region. The probability for this leakage is small, however at energies below 400 MeV the cross-section for single π^0 photoproduction is larger than for the $\gamma p \to n\pi^0\pi^+$ reaction by roughly three orders of magnitude. In order to reduce this background, first the missing mass was calculated under the hypothesis of single π^0 photoproduction; *i.e.* the π^+ candidate was assumed to be a recoil proton
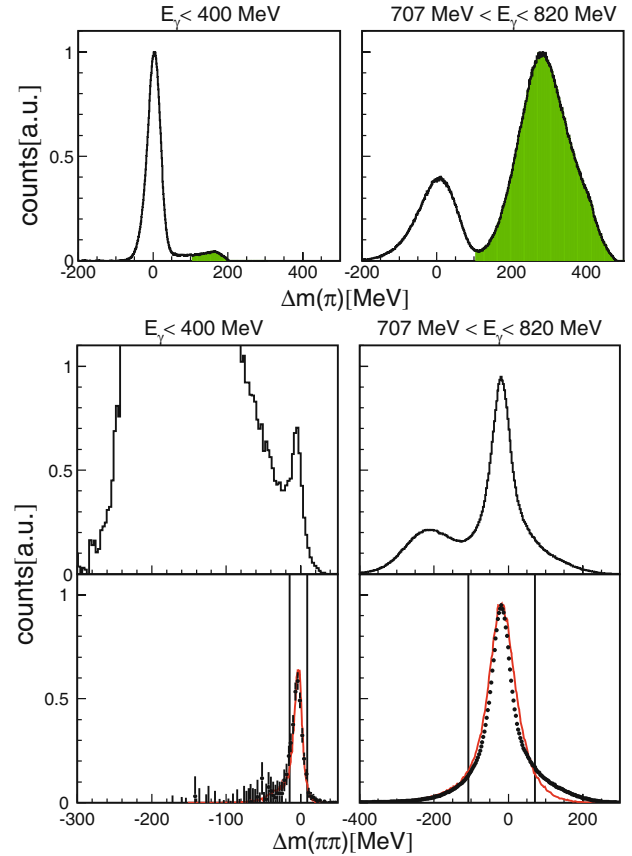
Fig. 7. (Color online) Upper row: missing mass calculated from the π^0 kinematics for the hypothesis of the $\gamma p \to p\pi^0$ reaction. The peaks centered around zero are related to background from this reaction. The shaded areas were selected for further analysis of the $\gamma p \to n\pi^0\pi^+$ reaction. Center and bottom row: missing mass calculated from π^0 and π^+ kinematics for the hypothesis of the $\gamma p \to n\pi^0\pi^+$ reaction. Center: all events. Bottom: after cut on shaded areas in $\Delta m(\pi)$. Solid (red) histograms: simulation of detector response. Vertical lines: applied cuts.

and the missing mass,

$$\Delta m(\pi) = |P_\gamma + P_p - P_{\pi^0}| - m_p, \qquad (7)$$

was formed. The result is shown in the upper row of fig. 7. In this spectrum, the background from single π^0 production sits in the peaks around zero, while events from $\gamma p \to n\pi^0\pi^+$ appear at large missing masses. For further analysis only the events in the shaded areas were accepted. The bottom row of fig. 7 shows the two-pion missing mass after this cut on the one-pion missing mass had been applied. These signals were practically background free with only a tiny contribution from $\eta \to \pi^0\pi^+\pi^-$ appearing at high incident photon energies and large missing mass. As for the double π^0 case the measured distributions agreed very well with the simulated line shapes.

At low incident photon energies there was another small, but significant background component that could not be removed completely with the invariant-mass analysis. It arises from the $\gamma p \to p\pi^+\pi^-$ reaction. Very slow π^-

mesons can be stopped inside the liquid-hydrogen target and then be captured by a proton to form pionic hydrogen. The pionic hydrogen can subsequently decay by charge exchange via the $\pi^- p \to n\pi^0$ reaction. Since this involves π^- that started with very low momenta, their energy loss is not significant within the experimental resolution and they cannot be discriminated by the missing-mass analysis. However, since the secondary π^0-mesons decay practically (within experimental resolution) at rest in the laboratory they can be eliminated in the pion kinetic-energy spectra (peak at zero energy) or even in the opening angle spectra of the pion decay photons (peak at $180°$).

In the final step again the kinetic energy and momentum of the recoil neutron were reconstructed from the reaction kinematics, regardless of whether the neutron was detected or not.

3.3 Extraction of cross-sections and systematic uncertainties

The absolute normalization of the cross-sections was based on the measurement of the incident photon flux, the target density, the two-photon-decay branching ratio of the π^0 which is $(98.823 \pm 0.034)\%$ [64], and the efficiency of the detector system.

The photon flux was determined as explained in sect. 2. However, for the present experiment an unsolved problem occurred in the read-out electronics, which led to a staggered pattern in all types of $N_d(E_\gamma)/N_\gamma(E_\gamma)$ ratios, where N_d are the counts for any reaction observed in the calorimeter and N_γ is the photon flux. The pattern occurred in groups of four tagger channels with a maximum amplitude of $\pm 3.6\%$. It was reduced to the average values by applying correction factors and a total systematic uncertainty of 5% was adopted.

The target surface density was 0.201 nuclei/barn with a systematic uncertainty of 2%. Contributions from the target windows (in total 125 μm Kapton) were determined with empty target measurements and subtracted. For the first part of the beam time, a build-up of ice on the downstream target window due to water permeation through the outer target tube was observed. The relative thickness of this layer was monitored using reactions with protons at large polar angles ($> 80°$), which can only arise from the heavy nuclei in the target windows and the ice but not from reactions on the liquid hydrogen. The track reconstruction with the MWPCs was used to measure the intensity of such events from the different windows. Subsequently, the results from a measurement with a water target, normalized to the thickness of the ice layers, were used to subtract this background. For the second half of the beam time, this problem was eliminated by a modification of the target. The correction for the $\pi^0\pi^0$ cross-section due to the ice layer for the first part of the beam time amounted to $\approx 10\%$. We estimate the total systematic uncertainty due to this correction is below the 2% level.

The systematic uncertainty due to the elimination of background via the invariant- and missing-mass analysis (including the agreement between the observed line shapes and simulations) is estimated to be about the $\pm 3\%$ level for the $\pi^0\pi^0$ final state and at $\pm 7\%$ for the $\pi^0\pi^+$ final state. It is larger for the latter due to the additional background from stopped pions undergoing charge exchange and because there is no invariant-mass filter for the charged pion.

The detection efficiency of the experimental setup was simulated with the GEANT3 program package [65]. All details of the experimental setup (active detector components as well as support structures and other passive materials) were included in the simulations and the results were tested in detail against known cross-section data. The detector response to electromagnetic showers induced by photons is very well known. The systematic uncertainty for single photon detection is so small, that even at very high statistical accuracy no significant deviations of cross-section data constructed from the $\eta \to 3\pi^0 \to 6\gamma$ decay from the world data base was observed [66]. This was exploited to increase the statistical quality of η-production data by simultaneous measurements of the 2γ- and 6γ-decay modes (see, e.g., [67]), again without observation of any systematic differences. For the charged pions, in addition the MWPCs must be considered, which are not routinely included in the GEANT simulation. They were treated in the following way. Efficiency and angular resolution of the chambers were experimentally determined (see sect. 3.1.2). In the simulation, position information from the chambers was generated according to these experimental parameters from the, in the simulation exactly known, tracks of the charged pions. Whenever such information was available it replaced in the analysis, like for the measured data, the position information from the CB cluster. If not, the MWPCs were ignored. For the detection efficiency of charged pions, this is only a second order effect. The efficiency is mainly determined by the GEANT3 simulation of PID and CB. The quality of GEANT3 simulations for charged pions in a calorimeter has been, for example, studied in [51], using the $\eta \to \pi^0\pi^+\pi^-$ decay. Also the agreement between the line-shapes of measured and simulated data (cf. fig. 7) demonstrates the high quality of the simulations.

The dominant uncertainty of the detection efficiency is related to the event generators used for the simulation, which should reflect the "true" kinematic correlations between the two pions. This is discussed in detail below. For the $\gamma p \to p\pi^0\pi^0$ reaction, two different event generators were used. The first generated events for a phase-space distribution of the $p\pi^0\pi^0$ final state (ps). The second generator, called "sequential" (seq), simulated the reaction chain $\gamma p \to \Delta(1232)\pi^0 \to p\pi^0\pi^0$ using a realistic-mass distribution for the $\Delta(1232)$. This was motivated by previous results [22, 25], indicating a significant contribution from decays of $N^\star$ resonances to the $\Delta(1232)$ intermediate state, which gives rise to invariant-mass distributions different from phase-space behavior.

From both simulations the detection efficiency was extracted as $\epsilon(E_\gamma, m(\pi\pi))$ and as $\epsilon(E_\gamma, m(\pi p))$, i.e. as a function of incident photon energy E_γ and the invariant mass $m(\pi\pi)$ of the pion pairs and the invariant mass
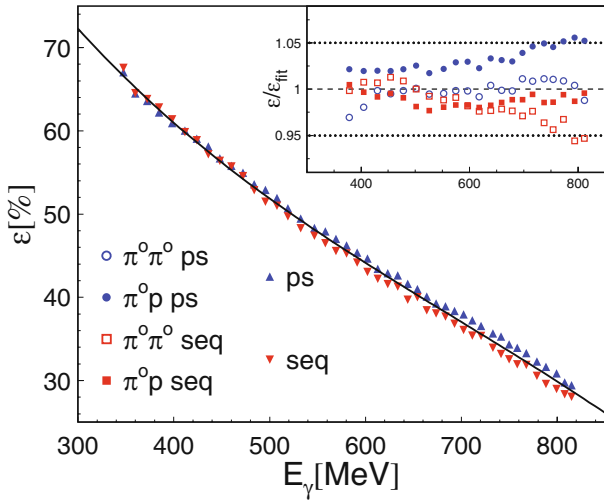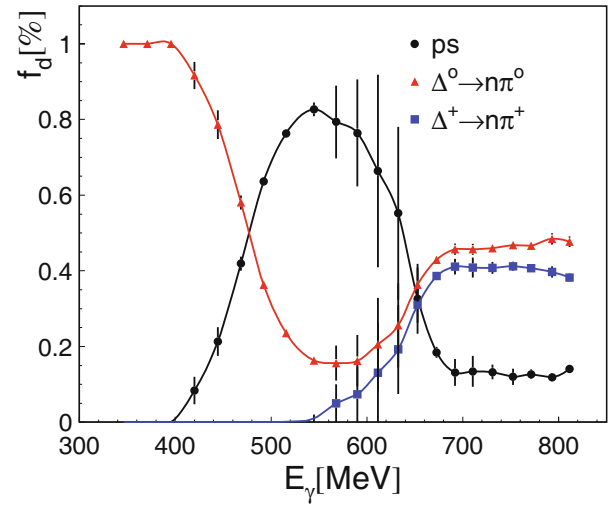
Fig. 8. (Color online) Double π^0 simulated detection efficiency for the $\gamma p \to p\pi^0\pi^0$ reaction. Main plot (blue) upward triangles: average of efficiency extracted from pion-pion and pion-proton invariant-mass distributions for phase-space event generator. (Red) downward triangles: same for sequential event generator. (Black) solid line: average of (ps) and (seq). Insert: deviation of all four efficiency curves from the adopted average.

Fig. 9. (Color online) Relative contribution f_d of phase-space (black dots), Δ^0 decays (red triangles) and Δ^+ decays to the invariant-mass distributions of $\gamma p \to n\pi^0\pi^+$. Symbols and curves represent the average of the fits for the $n\pi^0$ and $n\pi^+$ distributions; the error bars indicate their difference.

$m(\pi p)$ of the pion-proton pairs. For the latter, the two identical pions were randomized. Both types of invariant-mass distributions were then corrected with the appropriate detection efficiencies and the detection efficiency for the total cross-section computed by integration over the distributions. The results are summarized in fig. 8. Since the efficiencies obtained with the two different event generators differ only slightly, their average was used. As shown in the insert of fig. 8 the different results agree within $\pm 2\%$–$\pm 3\%$ at lowest incident photon energies and within $\pm 6\%$ at highest incident photon energies. We therefore estimate a systematic uncertainty rising from 3% at 310 MeV incident photon energy to 6% at 800 MeV. Some typical invariant-mass distributions are compared to the distributions used in the event generators and to previous data in fig. 10.

In a more recent measurement with the CB/TAPS setup at MAMI-C, published elsewhere [68], data for $2\pi^0$ production off the proton was also taken up to higher incident photon energies (1.4 GeV) and analyzed in a different way, using the kinematic-fit technique described in [66,69]. Due to this analysis and different trigger conditions, the detection efficiency was quite different from the present experiment (see fig. 8). For the range of incident photon energies discussed here, it was almost constant around 60%. The MAMI-C measurements did not reach the same statistical precision in the threshold region as the present results, but they can serve as an independent cross-check for systematic uncertainties.

The efficiency correction is more critical for the $\gamma p \to n\pi^0\pi^+$ reaction since in this case the charged pions were only accepted in the CB, which excludes a small part of the reaction phase-space and must be extrapolated by the ef-

ficiency simulations. For this reaction three different event generators were used: phase-space and the reaction chains,
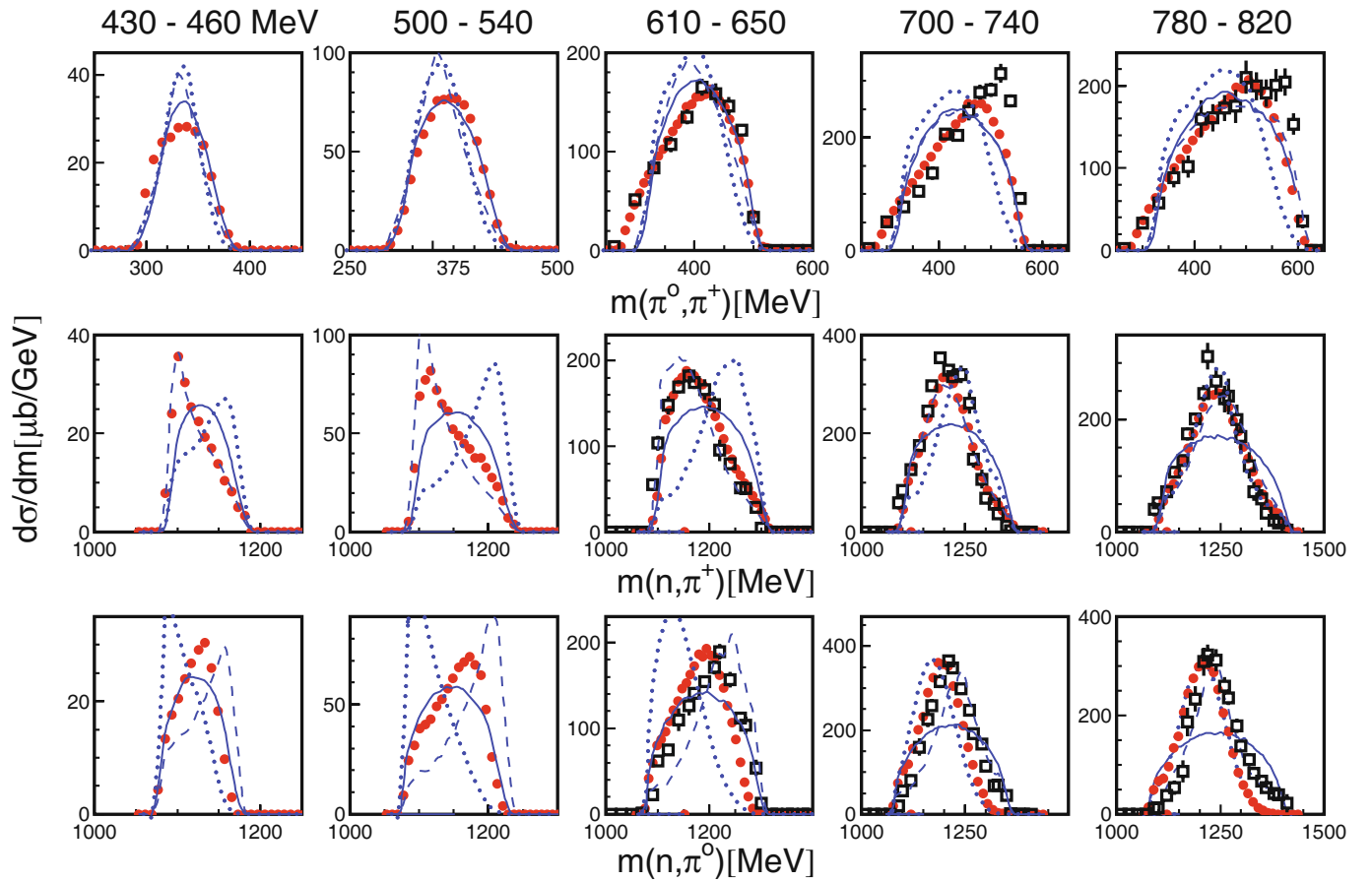
$$\gamma p \to \Delta^0(1232)\pi^+ \to n\pi^0\pi^+, \tag{8}$$

$$\gamma p \to \Delta^+(1232)\pi^0 \to n\pi^0\pi^+. \tag{9}$$

In a first step, the uncorrected invariant-mass distributions of the $n\pi^0$ and the $n\pi^+$-pairs were fitted with a superposition of the results from the three different simulations (the $\pi^0\pi^+$-pairs were much less sensitive to these reaction mechanisms). The relative contributions of these processes are summarized in fig. 9.

It should be emphasized that this analysis was only intended to construct a realistic detection efficiency. It does not include minor contributions like ρ-meson decays or interference terms. Nevertheless, the result reflects properly the main features of the $\gamma p \to n\pi^0\pi^+$ reaction. Close to threshold it is dominated by the $\gamma p \to \Delta^0(1232)\pi^+ \to n\pi^0\pi^+$ reaction chain. This is due to contributions from pion-pole and Δ-Kroll-Rudermann background terms, where a $\Delta^0\pi^+$-pair is produced at the first vertex and the Δ^0 subsequently decays into $n\pi^0$. Such diagrams, with the two pions interchanged, do not contribute, since the incident photon couples only to charged pions. The dominance of $\gamma p \to \Delta^0(1232)\pi^+ \to n\pi^0\pi^+$ at low energies is clearly visible in the invariant-mass distributions (see fig. 11). At the highest incident photon energies, contributions from sequential decays of $N^\star$ resonances become important. Since, due to isospin invariance, the $N^\star \to \Delta^0\pi^+ \to n\pi^0\pi^+$ and $N^\star \to \Delta^+\pi^0 \to n\pi^+\pi^0$ decays have the same probability, the contributions from Δ^0 and Δ^+ decays become comparable.
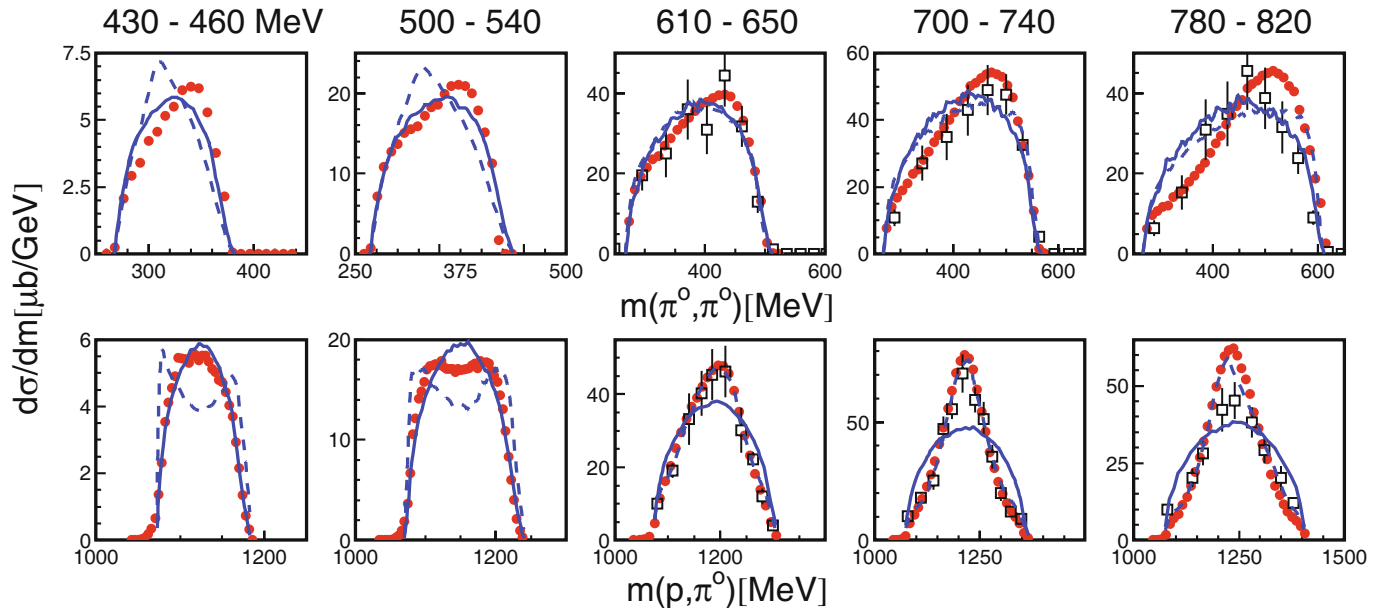
Fig. 10. (Color online) Typical invariant-mass distributions $m(\pi^0, \pi^0)$ and $m(p, \pi^0)$ for different ranges of incident photon energy for $\gamma p \to p \pi^0 \pi^0$. (Red) dots: present data. (Black) open squares: Wolf *et al.* [25]. Solid lines: phase-space. Dashed lines: sequential event generator.

Fig. 11. (Color online) Typical invariant-mass distributions (red) dots $m(\pi^0, \pi^+)$, $m(n, \pi^+)$, $m(n, \pi^0)$ for $\gamma p \to n \pi^0 \pi^+$. (Black) squares: Langgärtner *et al.* [27]. Solid lines: phase-space. Dashed lines: $\gamma p \to \Delta^0(1232)\pi^+ \to n\pi^0\pi^+$. Dotted lines: $\gamma p \to \Delta^+(1232)\pi^0 \to n\pi^0\pi^+$ event generators.
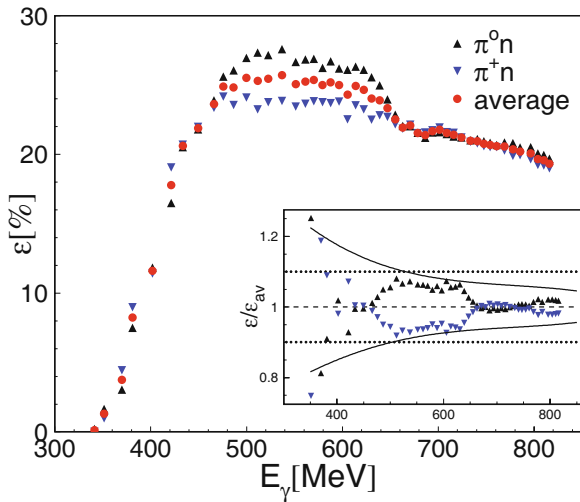
Fig. 12. (Color online) Detection efficiency for the $\gamma p \rightarrow n\pi^0\pi^+$ reaction. (Black) upward triangles: from invariant-mass distributions of $\pi^0 n$ final state. (Blue) downward triangles: from invariant-mass distributions of $\pi^+ n$ final state. (Red) dots: average. Insert: deviation from average. (Black) curves: assumed systematic uncertainty of efficiency correction.

Fig. 13. (Color online) Total cross-section of the $\gamma p \rightarrow p\pi^0\pi^0$ reaction in the immediate threshold region. (Red) dots: present measurement, open (black) triangles [25], open (blue) squares [28], (black stars) MAMI-C [68]. Solid line (dotted line): chiral perturbation theory prediction [2], eq. (1) (dotted line: eq. (1) with 0.9 nb). Dashed line: prediction from Valencia model [17]. Dash-dotted: model by Fix and Arenhövel [40]. Shaded (green) band at bottom: systematic uncertainty of present measurement.

In the intermediate energy range, where none of these processes is dominant, phase-space behavior parameterizes phenomenologically the contributions from many different diagrams. The results from the fits of the two different types of invariant-mass distributions are in quite good agreement for most of the energy range; only around $E_\gamma \approx 600$ MeV do larger deviations occur.
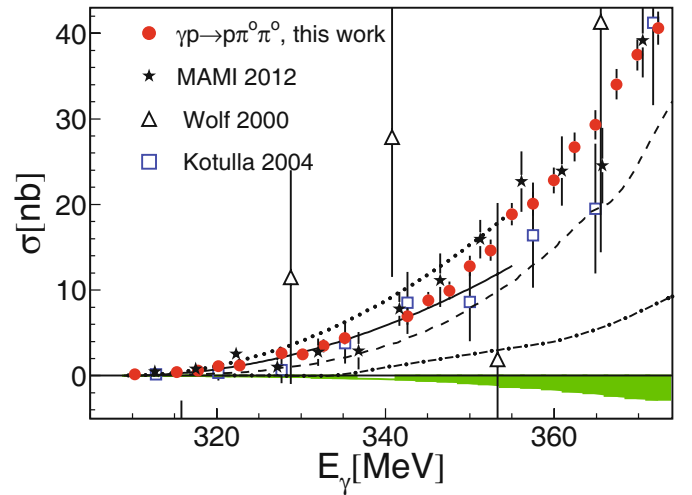
For the final efficiency simulations, event generators with a corresponding mix of the three contributions were used and, as in the $\pi^0\pi^0$ case, the detection efficiency was corrected as a function of the photon energy E_γ and the invariant mass of the particle pairs. As a check for systematic effects, this was done independently for the $\pi^0 n$ and $\pi^+ n$-pairs. The total detection efficiency was then again computed by integration. The result is summarized in fig. 12. The efficiencies obtained this way are in good agreement above $E_\gamma \approx 700$ MeV. They differ by up to $\pm 10\%$ at intermediate energies and by up to $\pm 20\%$ in the threshold region. For the final correction their average was used and the solid (black) curves in the insert of fig. 12 were assumed as systematic uncertainties, *i.e.* $\pm 5\%$ at 800 MeV and $\pm 20\%$ at 350 MeV.

In contrast to double π^0 production, the detection efficiency becomes very small in the threshold region because the charged pions are absorbed in the target or other material. Therefore it was not possible to analyze this reaction close to threshold.

4 Results and discussion

4.1 The threshold behavior

The total cross-section for double π^0 production in the threshold region is shown in fig. 13. The comparison

to previous results [25, 28] demonstrates the enormous progress achieved in experimental precision over the last decade. While the first measurements of this reaction [21, 22] could not extract any meaningful results for incident photon energies below 400 MeV, the data by Wolf *et al.* [25] from 2000 still have statistical uncertainties on the 100% level, the results from Kotulla *et al.* [28] reduced the uncertainties to the 50% level, and the present results pushed them below the 10% level (to the same magnitude as systematic uncertainties), allowing for the first time a stringent test of model predictions for this reaction. The more recent MAMI-C data do not reach the same statistical precision, but do not show any systematic deviation from the present results.

The measured cross-sections (fig. 13) are in excellent agreement with the prediction from chiral perturbation theory [2], using the central value for the s-wave coupling of the $P_{11}(1440)$ resonance to the double pion channel (eq. (1) with 0.6 nb). The calculation in the framework of the Valencia model by Roca *et al.* [17] somewhat underestimates the threshold data, whereas the results from the model of Fix and Arenhövel [40] (Two-Pion-MAID) are much lower.

Typical invariant-mass distributions for the threshold region are summarized in figs. 14 and 15. Very close to threshold (see fig. 14) pion-pion and pion-proton invariant masses behave like phase-space (blue, dashed curves). At slightly higher incident photon energies (see fig. 15) the pion-pion distribution is still similar to phase-space but develops some excess to large invariant masses. This is the typical energy range where in-medium modifications
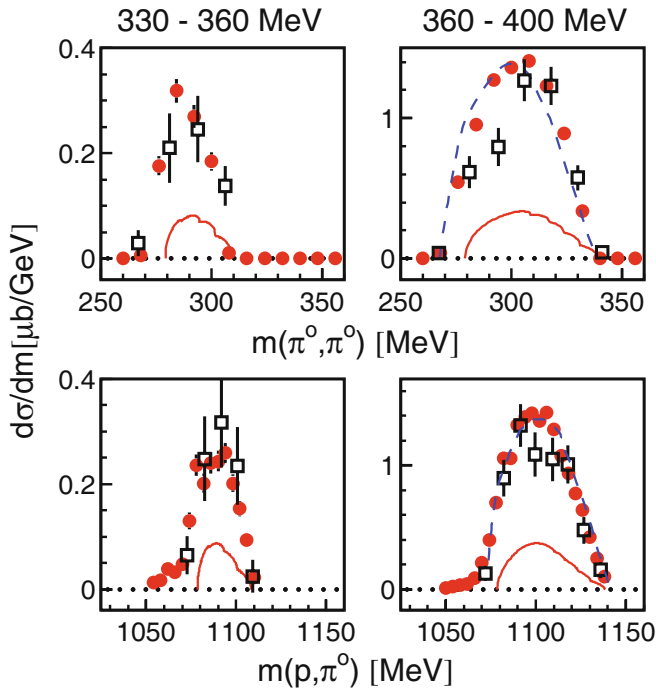
Fig. 14. (Color online) Invariant-mass distributions for $\gamma p \rightarrow p\pi^0\pi^0$ in the threshold region. (Red) dots: present measurement, (black) open squares Kotulla *et al.* [28]. Dashed (blue) curves: phase-space. Solid (red) curves: model of Fix and Arenhövel [40].
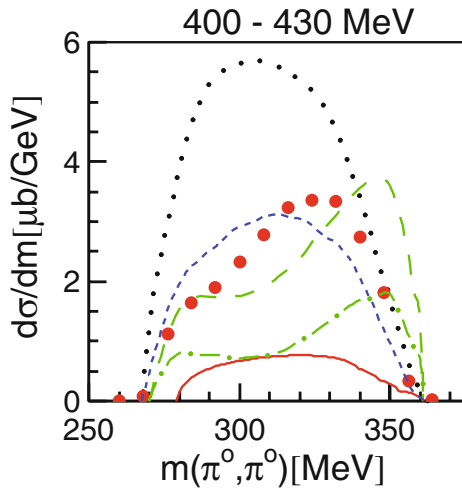
Fig. 15. (Color online) Invariant-mass distribution of the pion pairs from the $\gamma p \rightarrow p\pi^0\pi^0$ reaction. (Red) dots: present measurement. Curves show model results from: Bonn-Gatchina model [19] (black, dotted), Fix and Arenhövel [40] (red, solid), phase-space (renormalized in area, blue, dashed), Valencia model [17] (green, long-dashed with FSI, dash-dotted without FSI). Note: calculation from [17] is for $E_\gamma = 430$ MeV. It was renormalized by the ratio of the total cross-section at 430 MeV and the average of the total cross-section between 400 and 430 MeV.

have been searched for in quasi-free production off heavy nuclei [50,51]. The results from the reaction models are
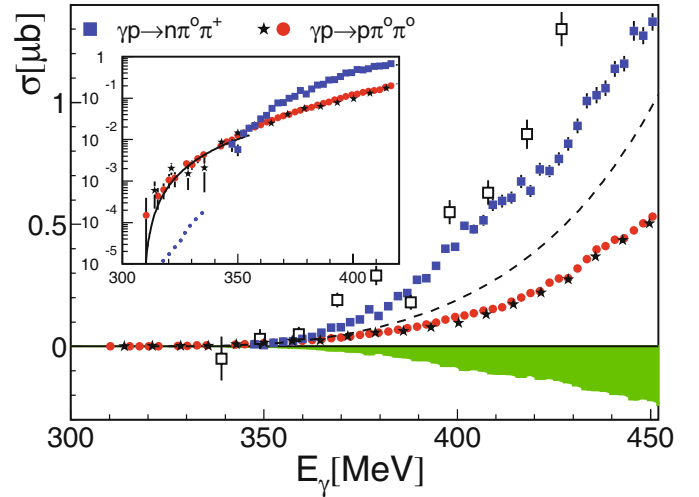
Fig. 16. (Color online) Comparison of the threshold behavior of the $\gamma p \rightarrow p\pi^0\pi^0$ and $\gamma p \rightarrow n\pi^0\pi^+$ reactions. (Red) dots: present measurement. (Black) stars: MAMI-C for $\gamma p \rightarrow p\pi^0\pi^0$. (Blue) squares present measurement, open (black) squares Langgärtner *et al.* [27] for $\gamma p \rightarrow n\pi^0\pi^+$. Dashed curve: Two-Pion-MAID model [40] for $\gamma p \rightarrow n\pi^0\pi^+$. Shaded (green) band: systematic uncertainty of the present $\gamma p \rightarrow n\pi^0\pi^+$ measurement. Insert: comparison on logarithmic scale. Solid (black) line: ChPT prediction for $\pi^0\pi^0$ [2]. Dotted (blue) line: ChPT prediction for $\pi^0\pi^+$ [1].

very different for this energy range. The BoGa analysis [19] resembles phase-space in shape but overestimates the data on an absolute scale. The prediction from the Two-Pion-MAID model [40], on the other hand, underestimates the data but also has a different shape. The calculation from Roca *et al.* [17] is closest to the data and also shows an accumulation of strength at high invariant masses, although this effect is slightly overestimated. The double-hump structure is due to an interference between the isospin $I = 0$ and $I = 2$ amplitudes, which is large and destructive in the Valencia model [17]. It is also noteworthy that the pion-nucleon final-state interaction in the $I = 0$ channel has a large effect on the cross-section in this model. It roughly doubles the result (compare dashed and dash-dotted curves in fig. 15) and effectively accounts for the loop-corrections in chiral perturbation theory. This effect is not included in the Two-Pion-MAID model and probably explains at least part of the missing strength in this model.

The threshold behaviors of $\gamma p \rightarrow p\pi^0\pi^0$ and $\gamma p \rightarrow n\pi^0\pi^+$ are compared in fig. 16. Unfortunately, it is not possible to measure $\gamma p \rightarrow n\pi^0\pi^+$ very close to threshold, since the low-energy charged pions do not reach the detector. The only alternative would have been to detect the neutral pion and the neutron and identify the reaction via overdetermined kinematics, but such events were not included in the trigger conditions (sum of energy deposited in Crystal Ball larger than 60 MeV, combined multiplicity of hits in Crystal Ball and TAPS three or larger). Over the range that could be investigated the cross-section is larger for the mixed-charge channel; however, at the lower
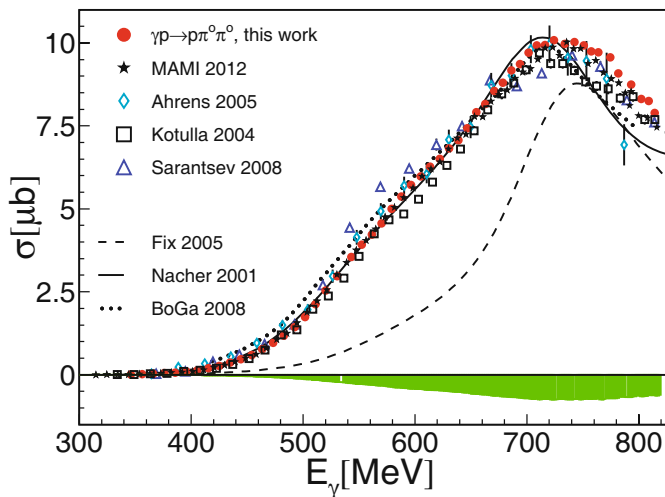
Fig. 17. (Color online) Total cross-section for the $\gamma p \rightarrow p\pi^0\pi^0$ reaction. (Red) dots: present measurement (shaded (green) band: systematic uncertainty). (Black) stars: MAMI-C [68]. (Black) squares: Kotulla *et al.* [19, 28]. (Blue) triangles: Sarantsev *et al.* [19]. (Cyan) diamonds: Ahrens *et al.* [33]. (Black) stars: new MAMI data. Solid curve: Valencia model (Nacher *et al.* [38]). Dashed curve: Two-Pion-MAID (Fix and Arenhövel [40]). Dotted curve: BoGa (Sarantsev *et al.* [19]).

limit of the accessible range there seems to be some indication for the cross-over predicted by chiral perturbation theory. A direct comparison to the predictions from chiral perturbation theory is not possible because they are limited to energies below 335 MeV (see insert of fig. 16). Also shown in fig. 16 is the prediction from the Two-Pion-Maid model [40], which again underestimates the cross-section, although not as dramatically as in the $\pi^0\pi^0$ case.

4.2 The resonance region

4.2.1 Total cross-sections and invariant-mass distributions

The total cross-section for double π^0 production is shown in fig. 17 and the invariant-mass distributions are summarized in figs. 18 and 20. The agreement between the present data and the MAMI-C data [68] is excellent over the whole energy range.
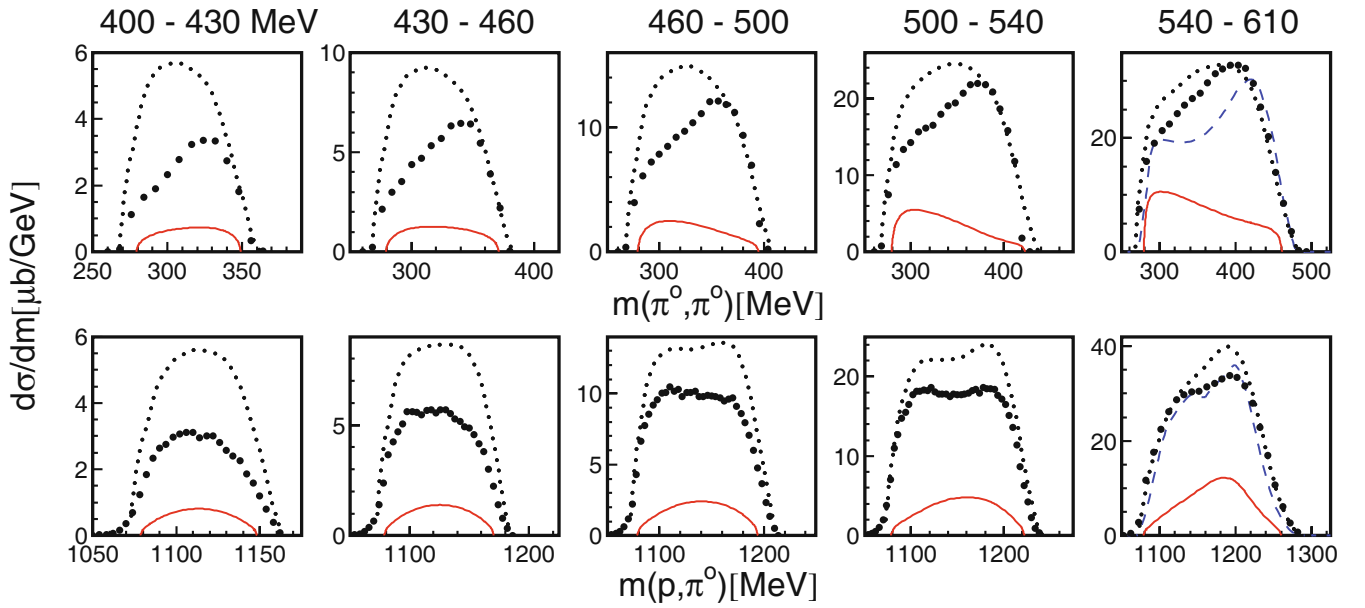
For the invariant-mass distributions only the present results are shown, since in most energy bins the MAMI-C data fall exactly on top of them. The total cross-section agrees within the systematic uncertainties with the earlier measurements with TAPS at MAMI [28], the GDH experiment at MAMI [33], and for most of the energy range (excluding a small region around 550 MeV) also with the Crystal Barrel experiment at ELSA [19]. For energies above 700 MeV, the present results are slightly higher than previous measurements, but also still within systematic uncertainties. Concerning the systematic effects it should be noted that only the present measurement

and the MAMI-C experiment detected the two pions over the full reaction phase space with fairly large efficiency (30%–70% for the present measurement (see fig. 8), $\approx 60\%$ in the MAMI-C case) and thus did not need any model-dependent extrapolations. This is reflected in the excellent agreement of the detection efficiencies simulated with different event generators and applied in different ways (see fig. 8). Furthermore, since detection of the recoil proton was not required, only the very well understood Monte Carlo simulation of electromagnetic showers induced from photons was needed for the efficiency calculation.

The agreement with the Valencia model [38] and the BoGa analysis [19] is comparable and clearly better than with the Two-Pion-MAID model [40]. The BoGa coupled-channel model was fitted (in addition to many other channels) also to the previous TAPS and CBELSA double π^0 data [19], so that reasonable agreement could be expected. Nevertheless, for incident photon energies below 600 MeV it overestimates the magnitude of the cross-section and does not agree well with the shape of the pion-pion invariant-mass distributions (fig. 18). In the same energy range the Two-Pion-MAID model [40] largely underestimates the magnitude and strongly disagrees with the shape of the pion-pion invariant-mass distributions. The Valencia model without FSI [16, 38] is in quite good agreement with the data already at incident photon energies above 550 MeV (see fig. 18), while below 450 MeV the influence of FSI is large (see fig. 15). All three models reproduce pion-pion and pion-proton invariant masses quite well at incident photon energies above 700 MeV, *i.e.* in the range where the reaction is supposed to be dominated by sequential resonance decays via the intermediate $\Delta(1232)$, the signal of which is clearly visible in the pion-proton invariant mass.

The total cross-section for $\gamma p \rightarrow n\pi^0\pi^+$ is shown in fig. 22 and the invariant-mass distributions are summarized in figs. 19 and 21. Agreement between the present and previous measurements is within their systematic uncertainties. The difference in the peak maximum around 750 MeV (also within systematic uncertainties) is probably due to the different procedures used for the simulation of the detection efficiencies. The procedure used in the present work is described in sect. 3.3, Langgärtner *et al.* [27] used a simple phase-space model, and Ahrens *et al.* [32] used the Valencia model [16]. For this channel, agreement with the results from the Valencia model [38] and Two-Pion-MAID [40] is comparable and for Two-Pion-MAID much better than for the double neutral channel. An analysis in the framework of the BoGa model is not yet available. At low incident photon energies the pion-nucleon invariant-mass distributions clearly show an enhancement of the $\Delta^0 \rightarrow n\pi^0$ decay from background terms (which is also reflected in an enhancement of small $n\pi^+$ invariant masses).

At higher incident photon energies the Δ signal appears in both pion-nucleon invariant masses as expected for sequential resonance decays. The build-up of strength at large values of the pion-pion invariant mass at the highest incident photon energies has been assigned to a contribution from ρ-meson decays [24, 27, 38, 40].
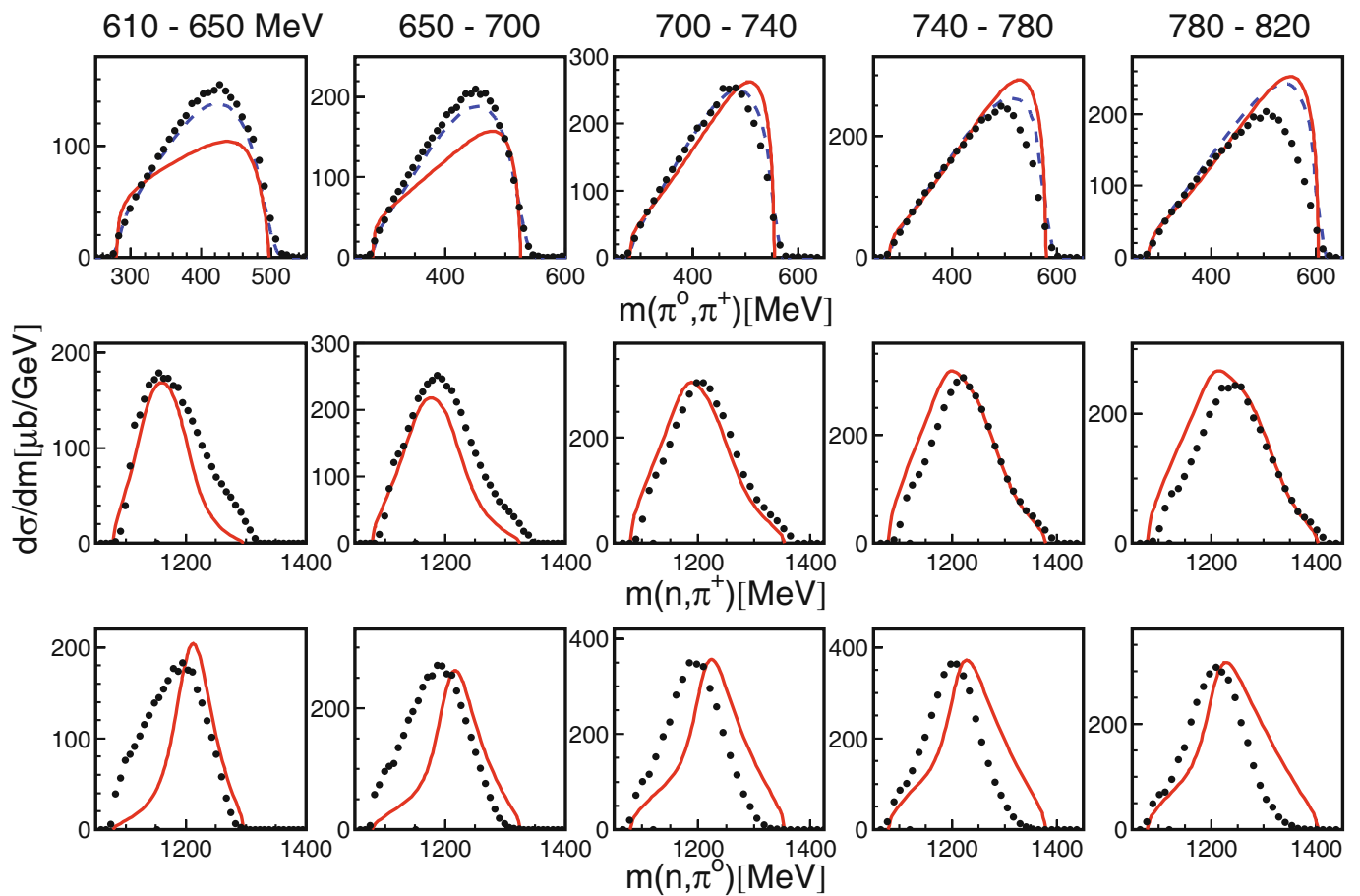
Fig. 18. (Color online) Invariant-mass distributions of pion-pion and pion-proton pairs for the $\gamma p \to p\pi^0\pi^0$ reaction for incident photon energies from 400–610 MeV. (Black) dots: present measurement. (Red) solid curves: Two-Pion-Maid model by Fix and Arenhövel [40]. (Black) dotted curves: BoGa analysis Sarantsev *et al.* [19]. (Blue) dashed curves: Valencia model Nacher *et al.* [38] (only available for the highest incident photon energy).
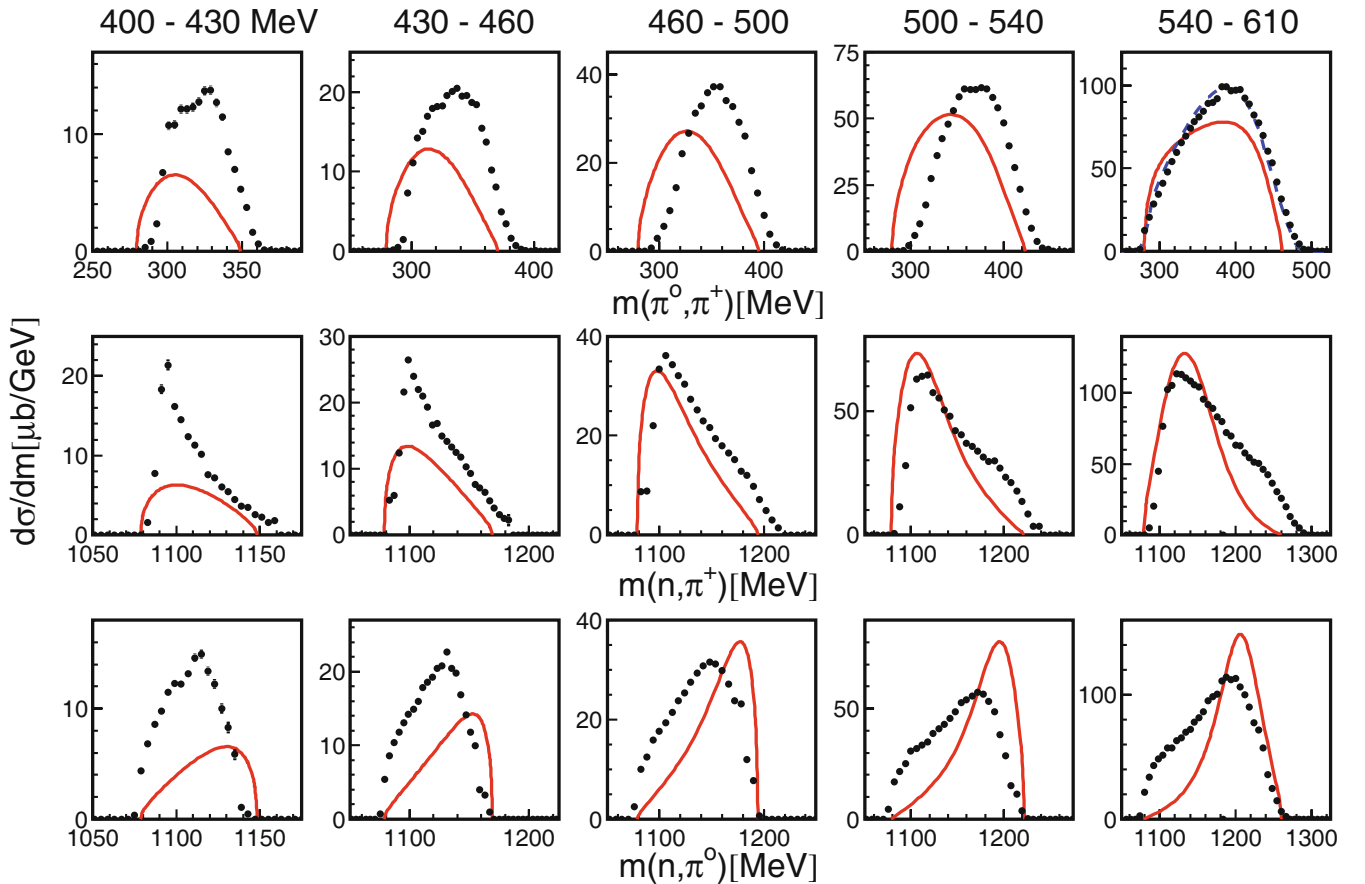

Fig. 19. (Color online) Invariant-mass distributions of pion-pion and pion-neutron pairs for the $\gamma p \to n\pi^0\pi^+$ reaction for incident photon energies from 400–610 MeV. (Black) dots: present results. (Red) solid curves: Two-Pion-Maid model by Fix and Arenhövel [40]. (Blue) dashed curve: Valencia model Nacher *et al.* [38] (only available the highest energy bin of pion-pion invariant mass).
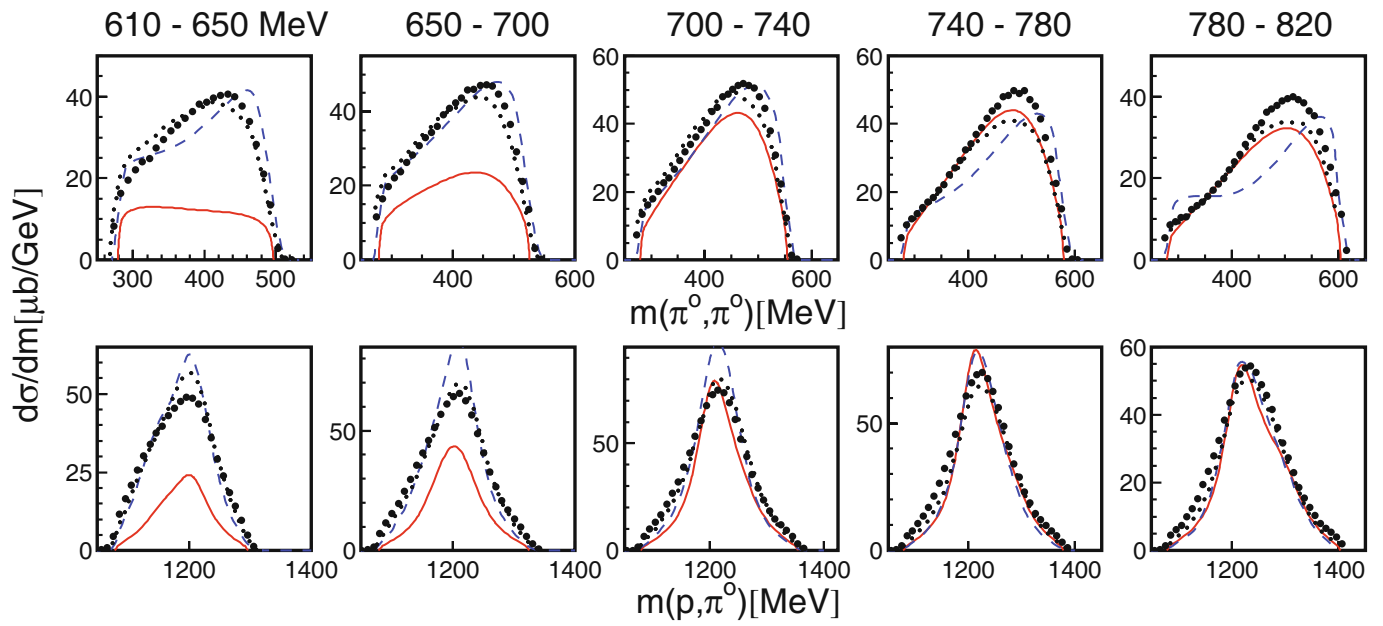
Fig. 20. (Color online) Invariant-mass distributions of pion-pion and pion-proton pairs for the $\gamma p \to p\pi^0\pi^0$ reaction for incident photon energies from 610–820 MeV. (Black) dots: present measurement. (Red) solid curves: Two-Pion-Maid model by Fix and Arenhövel [40]. (Black) dotted curves: BoGa analysis Sarantsev *et al.* [19]. (Blue) dashed curves: Valencia model Nacher *et al.* [38].

Fig. 21. (Color online) Invariant-mass distributions of pion-pion and pion-neutron pairs for the $\gamma p \to n\pi^0\pi^+$ reaction for incident photon energies from 610–820 MeV. (Black) dots: present measurement. (Red) solid curves: Two-Pion-Maid model by Fix and Arenhövel [40]. (Blue) dashed curves: Valencia model Nacher *et al.* [38] (only available for pion-pion invariant mass).
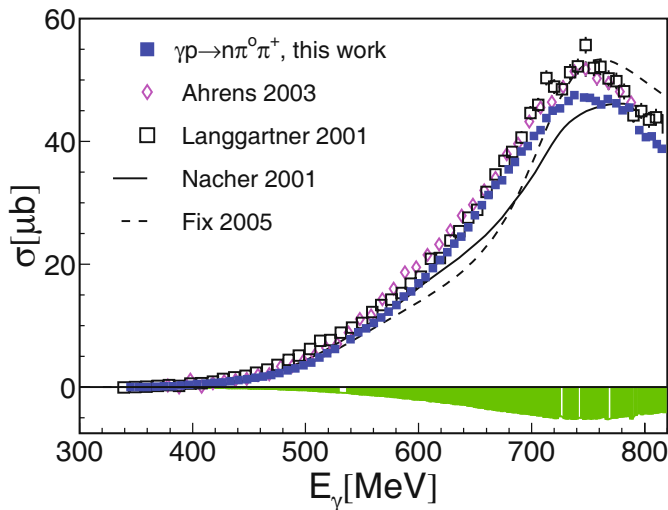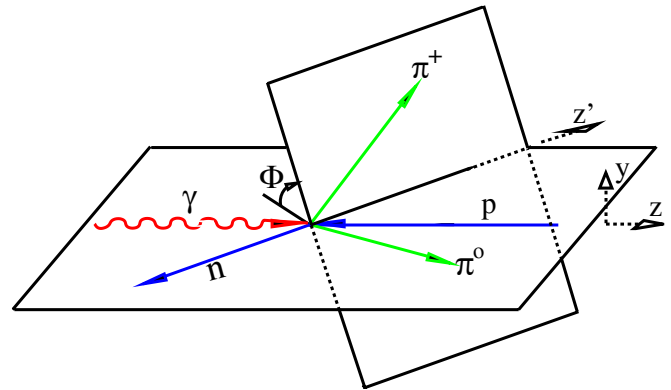
Fig. 22. (Color online) Total cross-section of the $\gamma p \to n\pi^0\pi^+$ reaction. (Blue) squares: present measurement (shaded (green) band at bottom: systematic uncertainty). Open (black) squares: Langgärtner et al. [27]. Magenta diamonds: Ahrens et al. [32]. Model results from Valencia (Nacher et al. [38]) and Two-Pion-Maid (Fix and Arenhövel [40]).

Fig. 23. Definition of the angle Φ between reaction plane (incoming photon and outgoing nucleon) and production plane (pion pair). For identical pions ($\pi^0\pi^0$-pairs) the role of pion one and two has to be randomized.
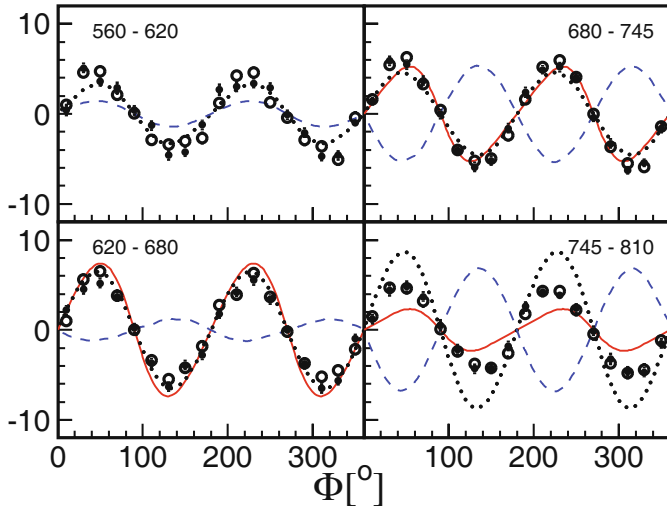
4.2.2 Beam helicity asymmetries

Several model predictions [39,40,70,71] indicate that polarization observables are extremely sensitive to the reaction mechanisms. So far experimental results are scarce. Beam asymmetries have been reported for the $\gamma p \to p\pi^0\pi^0$ [29] and $\gamma n \to n\pi^0\pi^0$ [30] reactions from the GRAAL experiment. The helicity dependence of the cross-sections has been measured with the Gerasimov-Drell-Hearn project at MAMI for the $n\pi^+\pi^0$, $p\pi^0\pi^0$, $p\pi^+\pi^-$, and $p\pi^-\pi^0$ final states [32–35]. The reaction models compare to all these data in a similar way as to the unpolarized data. The predictions from the Valencia model [16,38] and the Fix and Arenhövel model [40], without agreeing in detail with the data, reproduce the main features of the split into $\sigma_{1/2}$ and $\sigma_{3/2}$ components. The strong dominance of the $\sigma_{3/2}$ component observed for the $p\pi^0\pi^0$ final state [33] disfavors the Laget model [29] where the dominant contribution is from the Roper resonance. In this situation it came as a surprise when the first measurement of the beam helicity asymmetry of the $\gamma p \to p\pi^+\pi^-$ reaction at the CLAS facility [37] produced results that could not at all be reproduced by any reaction model.

The present experiment has confirmed this result and for the first time measured this polarization observable for the $\pi^0\pi^0$ and $\pi^0\pi^+$ final states. Results have already been published in a preceding letter [36]. Beam helicity asymmetries can be measured for reactions with at least three particles in the final state with a circularly polarized photon beam on an unpolarized target. The helicity asymmetry $I^\odot$ is defined by

$$I^\odot(\Phi) = \frac{1}{P_\gamma}\frac{\mathrm{d}\sigma^+ - \mathrm{d}\sigma^-}{\mathrm{d}\sigma^+ + \mathrm{d}\sigma^-} = \frac{1}{P_\gamma}\frac{N^+ - N^-}{N^+ + N^-}, \qquad (10)$$

where $\mathrm{d}\sigma^\pm$ is the differential cross-section for each of the two photon helicity states, and P_γ is the degree of circular polarization of the photons. For the extraction of the asymmetry $I^\odot(\Phi, \Theta_{\pi_1}, \Theta_{\pi_2}, \ldots)$ at fixed kinematical parameters the cross-sections $\mathrm{d}\sigma^\pm$ can be replaced by the raw count rates $N^\pm$ (right-hand side of eq. (10)) since all normalization factors cancel in the ratio. In principle, detection efficiency weighted count rates must be used for angle integrated asymmetries. However, due to the $\approx 4\pi$ coverage of the solid angle, detection efficiencies were rather flat in phase space at fixed incident photon energy, so that the effect of the efficiency corrections on the asymmetries turned out to be negligible. The photon beam was produced from bremsstrahlung of longitudinally polarized electrons. In the energy range of interest, polarization degrees P_γ between 60% and 80% were achieved. The angle Φ between reaction and production plane (see fig. 23) was constructed in the same way as in the work of Roca [71]. For the $\pi^0\pi^+$ final state, the pions were ordered as shown in the figure, i.e. Φ is the angle between the reaction plane and the part of the production plane with the charged pion. For the double π^0 final state their assignment was randomized, which means that the asymmetry must obey $I^\odot(\Phi) = I^\odot(\Phi + \pi)$. This was taken into account in the modeling, but not enforced in the data analysis.

The advantage of this polarization observable is twofold. It can be measured with good statistical quality (since only the electron beam must be polarized) and with small systematic uncertainties (since most uncertainties cancel in eq. (10)) and it is very sensitive to different contributions in the reaction models as has been demonstrated in [17].

The results for the $\pi^0\pi^0$ and $\pi^0\pi^+$ channels are summarized in figs. 24 and 25. Parity conservation enforces that $I^\odot(\Phi) = -I^\odot(2\pi - \Phi)$. This condition was not used in the analysis, but as indicated in the figures it is almost perfectly respected by the measurements.

The results for the double π^0 channel are in reasonable agreement with the Two-Pion-MAID model [40] and the BoGa analysis [19]. The results from the Valencia model [17] are completely out of phase with experiment.
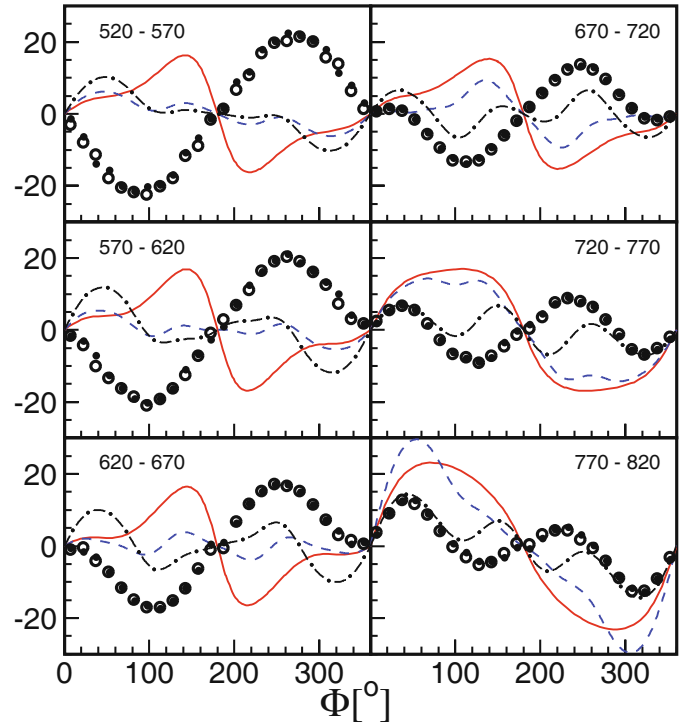
Fig. 24. (Color online) Beam helicity asymmetry for $\gamma p \to p\pi^0\pi^0$ for four different ranges of incident photon energy. Filled symbols: $I^{\odot}(\Phi)$, open symbols: $-I^{\odot}(2\pi-\Phi)$. (Red) solid curves: Two-Pion-MAID [40]. (Blue) dashed curves: Valencia model [17]. (Black) dotted curves: BoGa fit [19].

In the case of the $\pi^0\pi^+$ final state, no model reproduces the experimental results. This reaction is more complicated than $\gamma p \to p\pi^0\pi^0$, which is dominated in the models by sequential resonance decays while $\gamma p \to n\pi^0\pi^+$ has additional contributions from the ρ-mesons and also stronger contributions from non-resonant background terms. The predicted influence of such terms is shown in fig. 25 where for the Valencia model the full calculation and the result from a truncated model without the contributions from ρ-meson decays are compared. Surprisingly, inclusion of the ρ terms, which substantially improved the agreement for the total cross section and the invariant-mass distributions, has no positive effects for the asymmetry. The models do not even come close to the measurement. It is interesting to note, that for this reaction also the relative contribution of $\sigma_{3/2}$ and $\sigma_{1/2}$ components [32] is quite different in the Valencia and the Fix and Arenhövel model and for both of them agreement with experiment is worse than for the other isospin channels. This means that the reaction mechanisms are still not understood in detail.

5 Summary and conclusions

Precise cross-sections and beam helicity asymmetries have been extracted for the $\gamma p \to p\pi^0\pi^0$ and $\gamma p \to n\pi^0\pi^+$ reactions from the production thresholds up to the second resonance region.

In the threshold region the results support strongly the predictions from chiral perturbation theory [2]. The total cross-section for double π^0 production agrees with the ChPT prediction within statistical uncertainties. It supports also the value used in the ChPT calculation for the s-wave coupling of the $P_{11}(1440)$ resonance to the double π channel. The cross-section calculated in the framework of the Valencia model [17], taking into account πN

Fig. 25. (Color online) Beam helicity asymmetry for $\gamma p \to n\pi^0\pi^+$ for six different ranges of incident photon energy. Notation as in fig. 24 except for (black) dash-dotted curves: Valencia model [17] without ρ contributions. Results from BoGa are not available.

rescattering effects that resemble the loop corrections of ChPT, is also close to the measurement but underestimates it slightly outside the experimental uncertainties. On the other hand, the effective Lagrangian model (Two-Pion-MAID) from Fix and Arenhövel [40] underestimates the threshold cross-section typically by a factor of five. This underlines the large importance of πN rescattering for the double π^0 channel.

The results for $\pi^0\pi^+$ could not be directly compared to the chiral perturbation prediction. There is a gap of $\approx 15\,\mathrm{MeV}$ between the upper energy limit of the theory prediction and the lower energy limit of the experimental sensitivity. Nevertheless, below incident photon energies of $400\,\mathrm{MeV}$ the $\pi^0\pi^+$ excitation function bends downwards, seems to cross the $\pi^0\pi^0$ data around $350\,\mathrm{MeV}$, and could approach the ChPT threshold prediction. But it is of course desirable to close the gap, which in terms of cross-section spans almost two orders of magnitude, either by more refined ChPT calculations reaching higher incident photon energies or by more sensitive experiments. Altogether, the experimental results clearly support the ChPT calculations four threshold production of pion pairs.

The situation is much less clear at higher incident photon energies where the contributions from nucleon resonance decays become important. Fairly large discrepancies between experiment and model results and between different models occur in the intermediate energy range 400–650 MeV, where contributions from the $P_{11}(1440)$ resonance have been discussed [19]. In the $\pi^0\pi^0$ channel

the Two-Pion-MAID model [40] strongly underestimates the magnitude of the cross-section while the BoGa analysis [19] overestimates it. Both models disagree also in different ways with the shape of the invariant-mass distributions. Agreement for Two-Pion-MAID with the $\pi^0\pi^+$ results is better as far as the magnitude is concerned but also here the shape of the invariant-mass distributions is not well reproduced. The results for total cross-sections and invariant-mass distributions from the Valencia model are at least in reasonable agreement with experiment over the whole energy range. In the version including πN rescattering, the $\pi^0\pi^0$ invariant-mass distributions are quite well reproduced even at very low incident photon energies.

Finally, at the highest incident photon energies, in the second resonance region, all model analyses reproduce the absolute magnitude and the main features of the shape of the invariant-mass distributions for both isospin channels. However, the models still do not agree on the relative importance of the different contributions, *e.g.*, for the $D_{33}(1700)$ resonance to double π^0. The contribution of this state to $\pi^0\pi^0$ is very strong in the BoGa analysis, much smaller in Two-Pion-MAID, and almost negligible in the Valencia model.

As a new tool, beam helicity asymmetries, which had been predicted to be very sensitive to the details of the models, [71] have been measured with high precision. The result is surprising. The Valencia model, which had the best overall agreement with the measured cross-section, could not reproduce this observable for any of the isospin channels. Two-Pion-MAID and the BoGa analysis did much better for the double π^0 channel, but so far no model could reproduce the results for the $\pi^0\pi^+$ channel (an analysis in the framework of BoGa is not available for this channel). Therefore we must conclude, that so far none of the available reaction models correctly reflects the details of double pion photoproduction in the resonance region. Further efforts on the theory side are highly desirable.

References

1. V. Bernard *et al.*, Nucl. Phys. A **580**, 475 (1994).
2. V. Bernard, N. Kaiser, U.G. Meissner, Phys. Lett. B **382**, 19 (1996).
3. S. Dürr *et al.*, Science **322**, 1224 (2008).
4. J. Bulava *et al.*, Phys. Rev. D **82**, 014507 (2010).
5. R.G. Edwards *et al.*, Phys. Rev. D **84**, 074508 (2011).
6. S. Weinberg, Physica A **96**, 327 (1979).
7. J. Gasser, H. Leutwyler, Ann. Phys. **158**, 142 (1984).
8. E. Jenkins, A.V. Manohar, Phys. Lett. B **255**, 558 (1991).
9. V. Bernard, N. Kaiser, U.G. Meissner, Nucl. Phys. B **383**, 442 (1992).
10. R. Beck *et al.*, Phys. Rev. Lett. **65**, 1841 (1990).
11. M. Fuchs *et al.*, Phys. Lett. B **368**, 20 (1996).
12. A. Schmidt *et al.*, Phys. Rev. Lett. **87**, 232501 (2005).
13. A.M. Bernstein *et al.*, Phys. Rev. C **55**, 1509 (1997).
14. J. Ahrens *et al.*, Eur. Phys. J. A **23**, 113 (2005).
15. V. Bernard, N. Kaiser, U.G. Meissner, Nucl. Phys. B **457**, 147 (1995).
16. J.A. Gomez Tejedor, E. Oset, Nucl. Phys. A **600**, 413 (1996).
17. L. Roca, E. Oset, M.J. Vicente Vacas, Phys. Lett. B **541**, 77 (2002).
18. B. Krusche, S. Schadmand, Prog. Part. Nucl. Phys. **51**, 399 (2003).
19. A.V. Sarantsev *et al.*, Phys. Lett. B **659**, 94 (2008).
20. U. Thoma *et al.*, Phys. Lett. B **659**, 87 (2008).
21. A. Braghieri *et al.*, Phys. Lett. B **363**, 46 (1995).
22. F. Härter *et al.*, Phys. Lett. B **401**, 229 (1997).
23. A. Zabrodin *et al.*, Phys. Rev. C **55**, R1617 (1997).
24. A. Zabrodin *et al.*, Phys. Rev. C **60**, 055201 (1999).
25. M. Wolf *et al.*, Eur. Phys. J. A **9**, 5 (2000).
26. V. Kleber *et al.*, Eur. Phys. J. A **9**, 1 (2000).
27. W. Langgärtner *et al.*, Phys. Rev. Lett. **87**, 052001 (2001).
28. M. Kotulla *et al.*, Phys. Lett. B **578**, 63 (2004).
29. Y. Assafiri *et al.*, Phys. Rev. Lett. **90**, 222001 (2003).
30. J. Ajaka *et al.*, Phys. Lett. B **651**, 108 (2007).
31. M. Ripani *et al.*, Phys. Rev. Lett. **91**, 022002 (2003).
32. J. Ahrens *et al.*, Phys. Lett. B **551**, 49 (2003).
33. J. Ahrens *et al.*, Phys. Lett. B **624**, 173 (2005).
34. J. Ahrens *et al.*, Eur. Phys. J. A **34**, 11 (2007).
35. J. Ahrens *et al.*, Eur. Phys. J. A **47**, 36 (2011).
36. D. Krambrich *et al.*, Phys. Rev. Lett. **103**, 052002 (2009).
37. S. Strauch *et al.*, Phys. Rev. Lett. **95**, 162003 (2005).
38. J.C. Nacher *et al.*, Nucl. Phys. A **695**, 295 (2001).
39. J.C. Nacher, E. Oset, Nucl. Phys. A **697**, 372 (2002).
40. A. Fix, H. Ahrenhövel, Eur. Phys. J. A **25**, 115 (2005).
41. N. Bianchi *et al.*, Phys. Lett. B **325**, 333 (1994).
42. B. Krusche *et al.*, Phys. Rev. Lett. **86**, 4764 (2001).
43. V. Bernard, U.-G. Meissner, I. Zahed, Phys. Rev. Lett. **59**, 966 (1987).
44. F. Bonutti *et al.*, Phys. Rev. Lett. **77**, 603 (1996).
45. F. Bonutti *et al.*, Phys. Rev. C **60**, 018201 (1999).
46. F. Bonutti *et al.*, Nucl. Phys. A **677**, 213 (2000).
47. P. Camerini *et al.*, Nucl. Phys. A **735**, 89 (2004).
48. N. Grion *et al.*, Nucl. Phys. A **763**, 80 (2005).
49. A. Starostin *et al.*, Phys. Rev. Lett. **85**, 5539 (2000).
50. J.G. Messchendorp *et al.*, Phys. Rev. Lett. **89**, 222302 (2002).
51. F. Bloch *et al.*, Eur. Phys. J. A **32**, 219 (2007).
52. H. Herminghaus *et al.*, IEEE Trans. Nucl. Sci. **30**, 3274 (1983).
53. Th. Walcher, Prog. Part. Nucl. Phys. **24**, 189 (1990).
54. I. Anthony *et al.*, Nucl. Instrum. Methods A **301**, 230 (1991).
55. S.J. Hall, G.J. Miller, R. Beck, P. Jennewein, Nucl. Instrum. Methods A **368**, 698 (1996).
56. R. Novotny, IEEE Trans. Nucl. Sci. **38**, 379 (1991).
57. A.R. Gabler *et al.*, Nucl. Instrum. Methods A **346**, 168 (1994).
58. A. Starostin *et al.*, Phys. Rev. C **64**, 055205 (2001).

59. S. Schumann *et al.*, Eur. Phys. J. A **43**, 269 (2010).
60. D. Watts, in *Calorimetry in Particle Physics, Proceedings of the 11th International Conference, Perugia, Italy 2004*, edited by C. Cecchi, P. Cenci, P. Lubrano, M. Pepe (World Scientific, Singapore, 2005) p. 560.
61. G. Audit *et al.*, Nucl. Instrum. Methods A **301**, 473 (1991).
62. H. Olsen, L.C. Maximon, Phys. Rev. **114**, 887 (1959).
63. F. Zehr, PhD thesis, University of Basel (2010) unpublished.
64. K. Nakamura *et al.*, J. Phys. G **37**, 075021 (2010).
65. R. Brun *et al.*, GEANT, Cern/DD/ee/84-1 (1986).
66. E.F. McNicoll *et al.*, Phys. Rev. C **82**, 035208 (2010).
67. F. Pheron *et al.*, Phys. Lett. B **709**, 21 (2012).
68. V.L. Kashevarov *et al.*, Phys. Rev. C **85**, 064610 (2012).
69. S. Prakhov *et al.*, Phys. Rev. C **79**, 035204 (2009).
70. W. Roberts, T. Oed, Phys. Rev. C **71**, 055201 (2005).
71. L. Roca, Nucl. Phys. A **748**, 192 (2005).